LAGRANGIAN SCHLIEREN IMAGE VELOCIMETRY MEASUREMENTS IN EXHAUST PLUMES

by

RUDY MORALES

Submitted in Partial Fulfillment
of the Requirements for the Degree of
Master of Science in Mechanical Engineering
with Specialization in Explosives Engineering

New Mexico Institute of Mining and Technology
Socorro, New Mexico
August, 2018

ABSTRACT

Schlieren image velocimetry (SIV) is a non-intrusive flow visualization technique. SIV is the combination of schlieren optics and image processing methods to simultaneously characterize and measure the velocity fields of naturally occurring turbulent flow features. The focus of this work was image processing methods for SIV analysis. Image processing methods were explored with MATLAB to enhance the appearance of the turbulent flow features to convert them into optical particles. The optical particles were individually identified to determine their characteristics for subsequent tracking to measure velocities. With known parameters such as size, location, and centroid, filters were applied to isolate specified particles. Manual SIV was performed due to the limitations in an automated pattern recognition script to construct a path from the optical particles.

Here the SIV technique is applied to a free jet, a micro-turbine, and a small-scale liquid rocket engine to construct a velocity distribution in the exhaust plumes at various locations from the exit plane. Velocity distributions in the testbeds revealed similar trends to those of published data for free jets. Experimental results were limited to the lower velocity turbulent regions because SIV is only valid where the optical particles are present and visible in schlieren images.

Keywords: Non-intrusive flow visualization, turbulent flow features, Schlieren imaging, High-speed imaging, MATLAB, Exhaust plume characterization

ACKNOWLEDGMENTS

I would like to thank my advisor Dr. Michael J. Hargather and Stewart for encouraging me to to do a master's thesis even when I thought it was not possible. Everyone from the Shock and Gas Dynamics Lab for the help and making my time here enjoyable: Calla, Christian, Frank, John, Julio, Kyle B., Kyle W., Raj, Sara and Stewart. Jason and Richie from the EMRTC machine shop who help me make deadlines, on multiple occasions. My parents, brothers and rest of my family members who were always there for me. All the NMT faculty and staff members as well as the EMRTC staff and anyone else I may have forgotten. I know words cannot express how grateful I am and I know I don't say this as often as I should, but thank you all for helping me get to where I am today.

A portion of this research was supported at NMIMT through Sandia PO 1415058. Sandia National Laboratories is a multi-mission laboratory managed and operated by National Technology and Engineering Solutions of Sandia, LLC., a wholly owned subsidiary of Honeywell International, Inc., for the U.S. Department of Energy's National Nuclear Security Administration under contract DE-NA0003525

This thesis was typeset with LaTeX[1] by the author.

[1]The LaTeX document preparation system was developed by Leslie Lamport as a special version of Donald Knuth's TeX program for computer typesetting. TeX is a trademark of the American Mathematical Society. The LaTeX macro package for the New Mexico Institute of Mining and Technology thesis format was written by John W. Shipman.

CONTENTS

LIST OF TABLES

LIST OF FIGURES

This thesis is accepted on behalf of the faculty of the Institute by the following committee:

Dr. Michael J. Hargather

Dr. Tie Wei

Mark Grubelich

I release this document to the New Mexico Institute of Mining and Technology.

RUDY MORALES Date

CHAPTER 1

INTRODUCTION

1.1 Motivation

Currently there are limited methods that produce velocity measurements with simultaneous flow visualization. Methods such as Laser Doppler velocimetry are non-intrusive, but only provide localized point velocity measurements. Particle image velocimetry (PIV) is the most common quantitative flow field measurement, which supports full field velocity measurements and flow visualization, but it requires the use of seeding particles. Seeding particles with a dissimilar density from the fluid flow influence the reliability of the results. The selection and disbursement of seeding particles can be difficult or impossible in scenarios where the environment is not suitable such as electrohydrodynamic (EHD) flow [1, 2] or compressible flow. Situations like this provide a need for the development of non-intrusive flow visualization techniques that provide simultaneous quantitative flow velocity measurements. This thesis focuses on the exploration of non-intrusive flow visualization techniques to obtain qualitative and quantitative velocity data in flow fields.

1.2 Introduction

Fluid mechanics is the study of fluids at rest, in motion or the interaction of fluids in different phases [3]. Fluid mechanic studies include quantitative and qualitative methods such as numerical simulations and flow visualization techniques. The disadvantage of numerical simulations using computational fluid dynamics (CFD) is that they may require complex mathematics and intensive computational capabilities, depending on the complexity of the fluid flow. Once simulation are completed, experimental methods are often used to validate the results. Flow visualization techniques allow the ability to validate simulations by experimentally verifying the fluid characteristics in general, and velocity fields in particular [3].

1.3 Intrusive flow measurement methods

Intrusive flow measurement approaches require the use of physical objects such as tracer particles or instrumentation probes to be positioned directly within the flow. This inherently disturbs the flow and extensive approaches are made to minimize this intrusion or to use instruments that can be considered sufficiently small as to not disturb the flow. The primary intrusive methods include physical instruments like pitot probes and particle image velocimetry.

Velocity measurements in fluid flow may be obtained using intrusive physical instruments. Measurement instruments such as pitot tubes as shown in Figure 1.1 and hot-wire anemometers as shown on Figure 1.2 effectively obtain velocity measurements. These instruments only gather velocity measurements at a localized point and are typically impractical if the entire flow field is of interest. A concern with these measurement instruments is proper alignment with the fluid flow. Improper alignment can lead to skewed results since the pressure ports or sensor may only be partially exposed to the incoming fluid. Another disadvantage of the pitot tubes and hot-wire anemometers is that they do not provide any information for flow visualization.

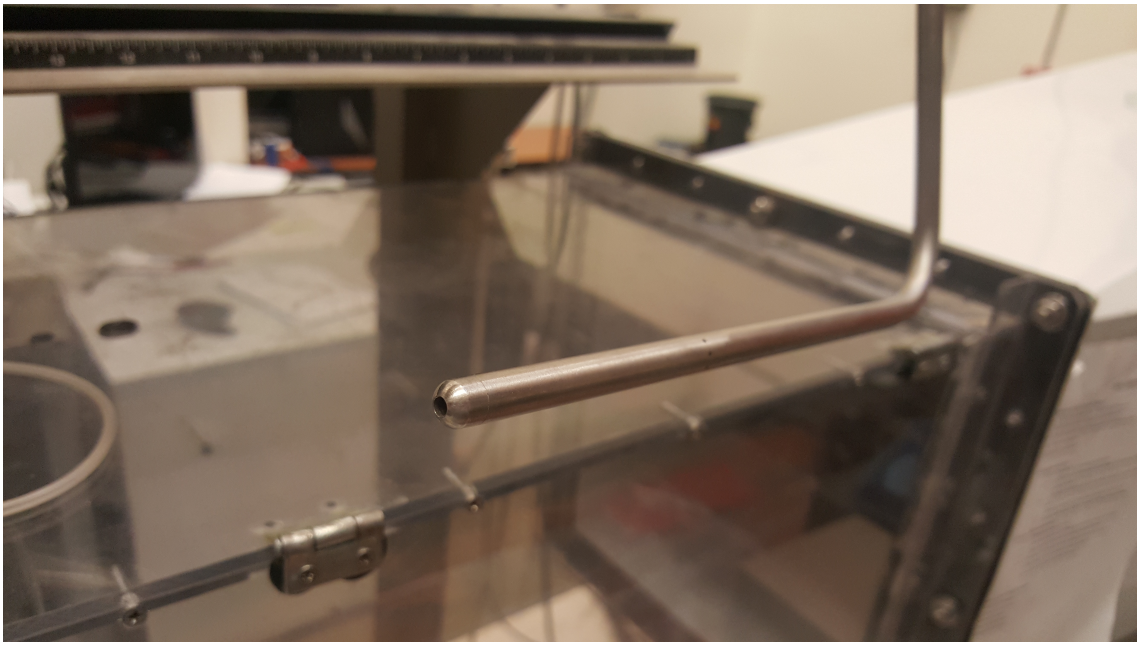

Figure 1.1: Pitot tube from a wind tunnel.

Figure 1.2: An example of a hot wire anemometer model number 407123 by EXETECH Instruments.

Intrusive flow visualization techniques have been used throughout the history of fluid dynamics research. A classic example is Ludwig Prandtl using mica as seeding particles in a water tunnel [4]. The water tunnel was used for qualitative analysis as the equipment required for quantitative measurement of particle motion was not available at the time [3]. The disadvantage of intrusive flow visualization is that it requires the use of seeding particles, which must be disturbed uniformly to get an adequate representation of the fluid flow. In order to obtain quantitative data from the water tunnel using flow visualization techniques such as optical equipment as well as computational hardware and software are needed.

Particle image velocimetry (PIV) is an approach that uses seeding particles, a camera and laser to measure velocities in a flow by tracking particle motion. The seeding particles are strategically injected in the fluid flow to ensure proper disbursement. A laser is used to create a 2D laser sheet to illuminate the region of interest. As the fluid passes through the region of interest, the laser sheet illuminates the seeding particles and a synchronized camera captures a pair of images. The series of image pairs is recorded then processed using PIV software. The PIV software tracks the displacement of the particles between two images. Typically the software matches unique interrogation windows from one frame to the surrounding areas in the subsequent frame using a cross-correlation algorithm. Once the new position of the particles is identified the displacement is computed, from which the velocity can be determined using the time separation of the images.

PIV is a useful flow visualization technique for field measurements. The

technique provides simultaneous velocity measurements and flow visualization. The disadvantage of PIV is that it requires the use of seeding particles such as dye, smoke, oil or micro spheres to be injected into the fluid [4]. The challenge is selecting seeding particles of similar density to the fluid to prevent any disturbances in the natural flow characteristics. Dissimilar densities between fluid and seeding particles influence the reliability of the results because the particles will lag or lead the flow due to their momentum difference from the flow. Not only may there be difficulty in injecting seeding particles, but ensuring that the particles are distributed uniformly in the flow field is also challenging. Inadequate particle distribution may result in under- or over-seeded flow regions, which can result in a lack of velocity measurement ability or over-exposure of camera images, respectively. Appropriately sized interrogation windows for cross-correlation must also be selected, to accurately resolve flow features of interest [4].

1.4 Non-intrusive flow measurements methods

The advantage of non-intrusive methods over intrusive methods is the ability to characterize the fluid flow without causing any disturbances in the naturally occurring features of the flow field. One non-intrusive method to obtain velocity measurements in fluid flow is Laser Doppler velocimetry (LDV). LDV uses two intersecting laser beams where the lasers cross defines the measurement volume [3]. Reflected light from the measurement volume is collected by a receiving lens and into a photo detector. The fluid flow causes a Doppler shift in the lasers resulting in interference fringes, which cause fluctuation in the photo detector and is correlated to a velocity. The limitation in LDV is that it only provides a localized point measurement and does not support flow visualization. It is also limited to transparent mediums, opaque mediums may cause full path obstructions and prevent the laser beam from reaching the receiving lens and photo detector [3].

1.5 Non-intrusive refractive imaging methods

Refractive imaging allows for simultaneous flow visualization with the ability to obtain velocity measurements non-intrusively. These methods are adaptable to various types of fluid flow, which allow the visualization of a range of disturbances in air from body heat to shock waves [5]. The disadvantage of refractive imaging is that it is limited to transparent mediums, since opaque mediums obstruct the light instead of refracting it.

Light refraction is the bending of light due to propagation through inhomogeneous mediums. Robert Hooke used the principle of light refraction to explain how the dissimilarities in the atmosphere cause stars to twinkle and to visualize heat haze on surfaces [5]. With the appropriate optical equipment refractive

imaging techniques can be applied to visualize fluid-flow phenomena. The optical diagnostic techniques that function on the principle of light refraction include schlieren imaging, background-oriented schlieren (BOS), and shadowgraphy.

Schlieren imaging is a non-intrusive optical diagnostic technique used to visualize refractive index gradients within a medium. The refractive index of a material is defined as the ratio of the universal speed of light in a vacuum to the speed of light in the medium [5]. Refractive index gradient arise as light is bent as it travels from a material with one refractive index to another. The refractive index of most materials is a function of material composition or chemical species, density, pressure, and/or temperature [5].

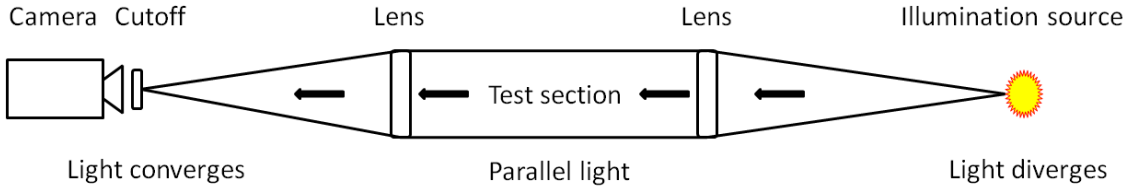

Figure 1.3: Schlieren imaging system schematic.

In a schlieren imaging system a point light source is used. The light is placed at the focal length of a parabolic lens to produce parallel light after passing through the lens. The light travels towards another parabolic lens which focuses the light onto a cutoff apparatus located at the focal point where it partially blocks some of the light [5]. When the object of interest is located between the two parabolic lenses, it refracts the light in many directions. The light that is refracted travels through the parabolic lenses and onto the cutoff apparatus, which blocks some of the light rays. Figure 1.3 schematically demonstrates a schlieren system. Light rays are refracted perpendicular to the gradient of the refracted index. The cutoff apparatus is placed in an orientation to maximize the interaction with the refracted rays of interest. A cutoff placed in the vertical position is used to visualize the horizontal refractive index gradients [5]. The light that passes by the cutoff enter the camera and produces the schlieren image of the object.

BOS or synthetic schlieren [6] is a flow visualization method that uses digital image processing routines to visualize refractive disturbances. The BOS method uses a background with a non-uniform features, like that of a random speckle pattern against which refractive disturbances are imaged. The event or object of interest causes disturbances in the refractive index and distorts the appearance of regions in the background. An image is taken before the event prior to any distortions called a tare image. Image processing techniques are then used to compare the tare image and the test image resulting in a newly reconstructed

image that displays distorted regions. The BOS method is useful in large-scale explosives field tests to visualize and track the position of the shock wave to determine various properties [7].

The shadowgraph method is similar to that of schlieren imaging, but images the second derivative of the refractive index field. Typically, shadowgraph is implemented with non-parallel light in the test section. The retroreflective shadowgraph method uses an illumination source, a camera, a 45° rod mirror lens adapter and a reflective screen [8]. The illumination source is aimed at the rod mirror in front of the camera and projects light onto the screen. As the light passes through the object of interest, it refracts the light. The refracted light increases the illumination in the new position while the illumination in the previous position decreases [5]. The shadowgraph method is less sensitive to disturbances in the refractive index than the schlieren system as it visualizes the second spatial derivative of the refractive index [5]. Shadowgraph is applicable to small-scale testing were explosive are studied for geometry such as sphericity, the issue with shadowgraph is that the test region is in diverging light, which must be accounted for during the analysis [8]. Focused shadowgraph imaging is performed using schlieren optics, but with no cutoff in place. This allows parallel light through the test section, but images the second derivative of the refractive index field.

1.5.1 Schlieren image velocimetry (SIV)

Schlieren image velocimetry (SIV) is the combination of schlieren optics and cross-correlation methods, to measure the velocity profile of the flow field by tracking the motion of naturally occurring turbulent flow features [9]. SIV is a non-intrusive method since schlieren optics do not interfere with the fluid flow. Like PIV, SIV provides simultaneous velocity measurements and flow visualization of the entire flow field. Since there are no tracer particles needed, the turbulent features are the objects of interest. Schlieren images produce a 2D path average of the fluid flow. The images require pre-processing techniques to enhance the quality of the turbulent features and reduce the background noise. After the images are pre-processed, cross-correlation methods are applied to obtain velocity measurements. Like PIV, adequate and uniformly distributed seeding particles in the flow field are desired: for SIV, turbulent feature dense images are desired. SIV is limited to transparent mediums and turbulent flow, if the flow is not sufficiently turbulent as shown on Figure 1.4 there would not be sufficient unique turbulent features to perform correlations on.

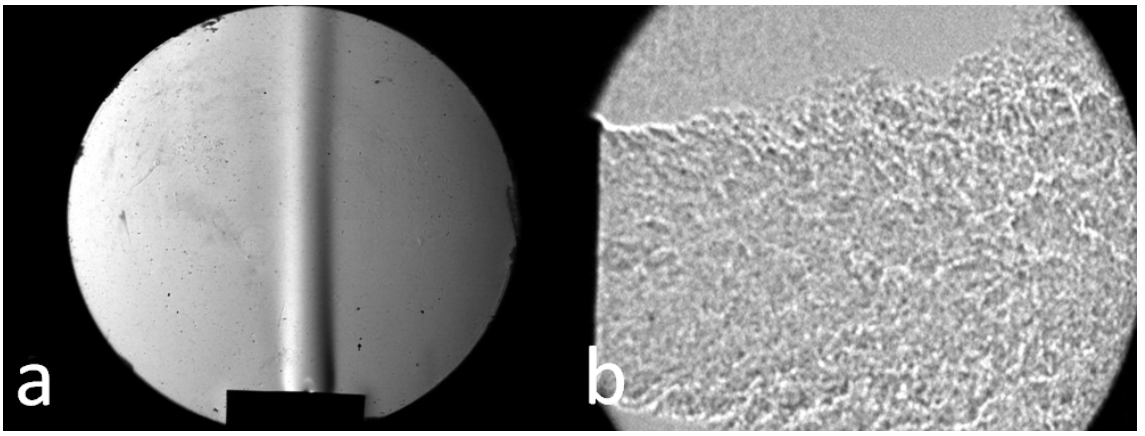

Figure 1.4: (a) Schlieren image of a candle with a vertical cutoff.This is an example of laminar flow and thus is not suitable for SIV because there are no unique features to track, like those in turbulent flow.(b) Focused shadowgraph image of the micro-turbine, using schlieren optics with no cutoff.

Most SIV studies have been performed using parallel light schlieren with either a lens or mirror based system [1, 2, 9–12]. Parallel light schlieren produces a 2D path average image were the average light refracted through the flow field is visualized. The issue with a path average schlieren image is the intermittent appearance of the turbulent features. This is an issue for the image correlation because the features may disappear and causes loses of correlation. In an attempt to isolate a section within the depth of field and address the issue of overlapping features, focusing schlieren has been tested. Unfortunately, a focusing schlieren image has insufficient features to track [11, 13]. This is similar to an under seeded condition exhibited by PIV where there are insufficient seeding particles to track [4]. Gogineni and Kweon used a helium jet with water injection in order to mimic the spray pattern of an injector like those used in combustion engines. The injection of water into the helium resulted in distorted images which resulted in poor results [13].

Emishaw et al applied BOS to a centrifugal blower to obtain velocity measurements. The fluid was seeded using a heater to create a gradient in the density and the index of refraction [14]. Other studies with BOS have been performed by Tokgoz et al, which tested an elliptical jet in a water tank with seeding particles in order to test simultaneous BOS and PIV. The challenges brought with simultaneous BOS and PIV is the visibility of the seeding particles when the camera is used to focus on the particles or the shadow on the screen [6]. Papadopoulos used a synthetic particle field to visualize a flame with a co-annular burner. The issues with the synthetic particle field was the misalignment of the two separate lasers used to achieve the temporal resolution [15].

Jonassen et al evaluated the cutoff of the schlieren system to quantify the setting that produced the most feature dense images for SIV. The cutoff apparatuses tested included: horizontal, vertical, circular and focused shadowgraph (no cutoff). The results from the study identified uneven illumination caused by

the orientation of the cutoff resulted in poor measurements [12]. The application of 10-20% cutoff resulted in insufficient features displayed. Over 90% cutoff resulted in suppression of features due to the over-saturation of darkness. The optimal cutoff was found to be between 30-60%, this region allows for the visualization of the smaller and larger features. Biswas and Qiao tested a helium jet in the vertical position with a variation of cutoff orientations. The vertical cutoff was found to perform poorly due to the uneven illumination of the fluid flow, this was due to the perpendicular position of the cutoff to the exit plane of the helium jet [10].

In some studies the high-speed camera were used to replace the synchronization of the illumination source and PIV camera [12, 16]. The issue with the traditional PIV camera and laser system is that it may produce blurred images depending on the velocity of the measured fluid flow [11, 12, 16]. The misalignment of using multiple lasers to achieve the temporal resolution needed also causes issues [15]. High speed cameras have the capabilities to capture images at frame rates in the thousands and even millions of frames per seconds at a reduced resolution [10, 12].

Various types of lasers such as nd:YAG and white-light emission of a laser-induced air or argon spark breakdown were used in research studies[12, 16]. The difficulty in using the laser system as an illumination source is that it introduces coherent artifact noise into the schlieren images [12, 16]. In another research study, an arc lamp was tested [10], but an LED was found to produce sufficient light to illuminate the features in the flow [11, 12, 16].

SIV was applied to various test subjects that ranged from helium jets and wind tunnels at sub-sonic and supersonic velocities. Most comparisons in research studies were made using traditional PIV measurements. Other comparisons were made using physical instruments such as pitot tubes. Theoretical performance results of the system were calculated and compared to experimental results as well [10–12].

Arnaud et al. mathematically estimated the flow velocity around a heated cylinder with natural and forced convection. The Gladstone-Dale constant was used to correlate the density to the pixel intensity [5]. From the calculated density, the velocity of the flow field was determined using the continuity equations. The image demonstrated qualitative features such as vortices but resulted in inaccurate velocity measurements due to the poor quality of the images [17].

Manual image correlation was attempted as early as 1936 by Townend, who used shadowgraph and schlieren images to manually track the displacement of turbulent features to obtain velocity measurements [18]. Hargather et al used manual SIV where two consecutive frames were used and features were tracked by hand to obtain velocity measurements. This is a tedious method and introduces human error into the calculation [9].

Most all of the results from SIV resulted in the lower velocities than the PIV measurements, physical measurements or theoretical data. From the results, the PIV software is not suitable to track the turbulent features. The PIV identifying and tracking algorithm was found to be suitable for an ideal particle size of

2-3 pixels in diameter and about 4 particles per interrogation window [12]. Intermittent frequency and deformation of the turbulent features leads to loss of correlation. This is due to the path average image of the axisymmetric flow in the schlieren images [9, 11, 19].

1.5.2 Image processing techniques

In an effort to enhance, the quality of the images before being processed by PIV software, image processing techniques were applied to the schlieren images. Multiple research studies tested techniques to isolate the features from the background [9–12]. Of particular note are Hargather et al. who applied background subtraction by averaging the images in the data set and subtracting it from each individual image [9] and Biswas et al. who performed a binary conversion to apply edge detection and create synthetic seeding particles from turbulent features [10].

Poor performance of the commercial PIV software programs with the schlieren images [6, 9–12], led to the development of a MATLAB script better suited for the turbulent features [9]. The MATLAB script uses the built in function *normxcorr2* which uses template matching. A section of an image is selected in one frame and the algorithm finds the location of best match in another frame. The velocity measurements from the customized MATLAB script improved over the PIV software but were still lower than measurements made with a pitot tube. Further processing with the Abel transform was used to reconstruct the center-plane velocity from the path-averaged schlieren measurement and provide an accurate comparison [9–12].

Biswas and Qiao applied image pre-processing techniques to reduce the signal to noise ratio and reconstruct the image [10]. Contrasts adjust and threshold were set to perform edge detection of the turbulent features and create binary images. The newly reconstructed images were processed with robust phase correlation (RPC) and quantum imaging (QI) methods [10].

1.6 Research goals

The goals of this thesis are to develop new image processing and correlation methods for SIV. Image pre-processing techniques are applied to the raw schlieren images using MATLAB to identify and isolate the turbulent features in an effort to reduce the signal to noise ratio. Manual turbulent feature tracking was performed, since the chaotic behavior of the turbulent features cause complications in the pattern recognition algorithm. Manual turbulent feature tracking facilitates the ability to focus on coherent turbulent features to build trajectory paths.

CHAPTER 2

EXPERIMENTAL SETUP

This section provides an overview of the schlieren system, testbeds and the equipment used to perform the experiments for this research. All testbeds produced flow characteristics that are self-seeding for SIV and cover a range of velocity measurements from subsonic to supersonic flow.

2.1 Schlieren imaging system

The schlieren system used for all experiments was a lens based, parallel light system. Various parabolic lenses were used to produce parallel light, but all lenses had a diameter of 127 mm. All optical equipment was mounted on a Ealing optical rails, with mounts and optical rods to provide adjustment and reduce alignment issues. A Newport optical table with vibration control capabilities was used when possible, but in field tests other methods to secure the optical equipment were used. A schematic of the schlieren system used for all testbeds is shown on Figure 1.3. The schlieren system for the micro-turbine and small-scale liquid rocket engine test were mounted using wooden tables as shown on Figure 2.1 and Figure 2.2.

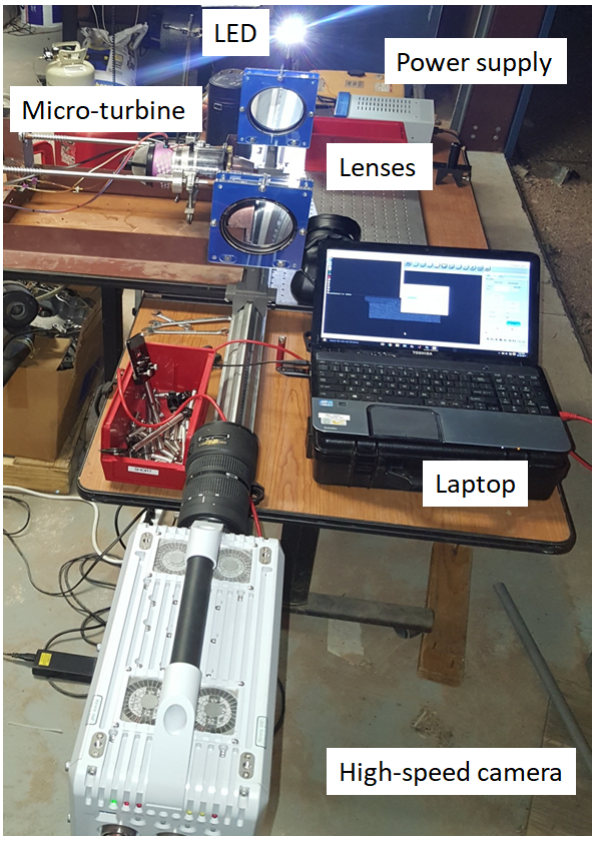

Figure 2.1: Lens based schlieren system for the micro-turbine.

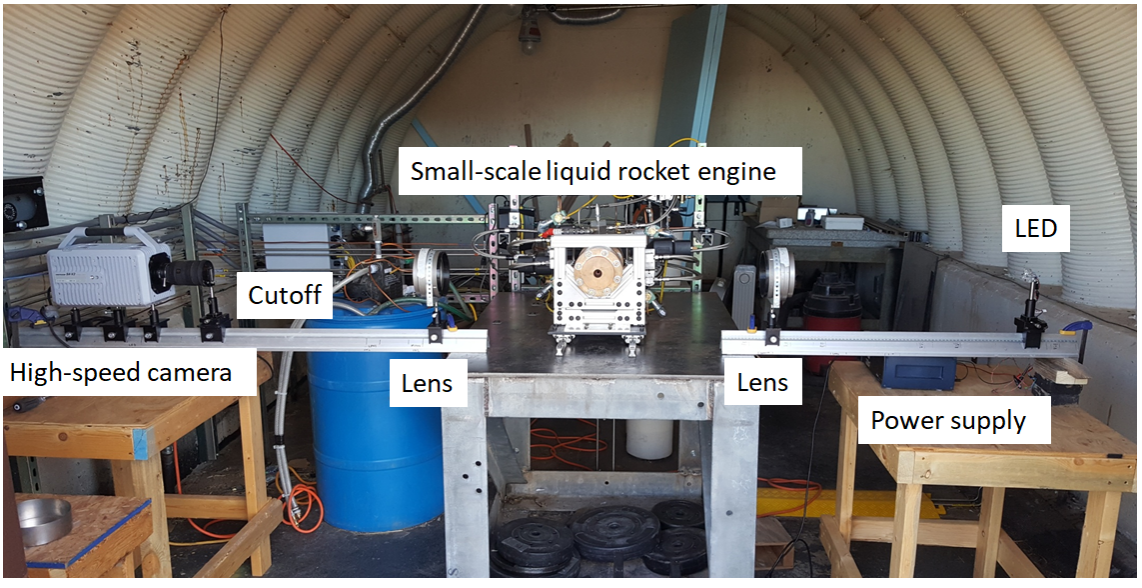

Figure 2.2: Lens based schlieren system for the small-scale liquid rocket engine.

Two cameras were used to record the tests: Photron FASTCAM SA-Z (color) and Photron FASTCAM SA-X2 (monochrome). The SA-Z provided the fastest frame rate at the best resolution of 512x256 pixels at 120,000 frames per seconds (fps) with a shutter speed of 0.16 μs, but is a color camera and requires additional data storage compared to the SA-X2. The SA-X2 was the camera of choice due to the monochrome sensor although it only allowed for 120,000 fps and a shutter speed of 0.29 μs at a resolution of 256x280. Monochrome cameras were preferred over color cameras due to increased sensitivity. The monochrome camera imaging also allows for faster image processing because there is only a single plane of pixel information.

Multiple cameras were selected throughout the series of test conducted based on the availability. For the helium jet images were recorded using the Photron FASTCAM SA-Z and the FASTCAM SA-X2. For the micro turbine the Photron FASTCAM SA-X2 was selected. The Photron FASTCAM SA-X2 was used for the small-scale liquid rocket engine. The camera settings for each testbed are shown in Table 2.1

The camera lenses were chosen based on the size of the testbeds. For the helium jet tests an 80-200mm Nikon zoom lens was selected. For the micro turbine, an 18-55mm Nikon zoom lens was used and for the small-scale liquid rocket engine a 28-70mm Sigma zoom lens was used.

Table 2.1: Camera settings for individual testbeds

Testbed	Spatial resolution (pixels)	Frame rate (fps)	Exposure (μs)	Camera
Helium jet	384x256	150,000	0.16	SA-Z
Micro-turbine circular cutoff	384x256	100,000	0.29	SA-X2
Micro-turbine horizontal cutoff	384x256	100,000	0.29	SA-X2
Micro-turbine shadowgraph	384x256	100,000	0.29	SA-X2
Micro-turbine vertical cutoff	384x256	100,000	0.29	SA-X2
Small-scale liquid rocket engine	384x160	150,000	0.29	SA-X2

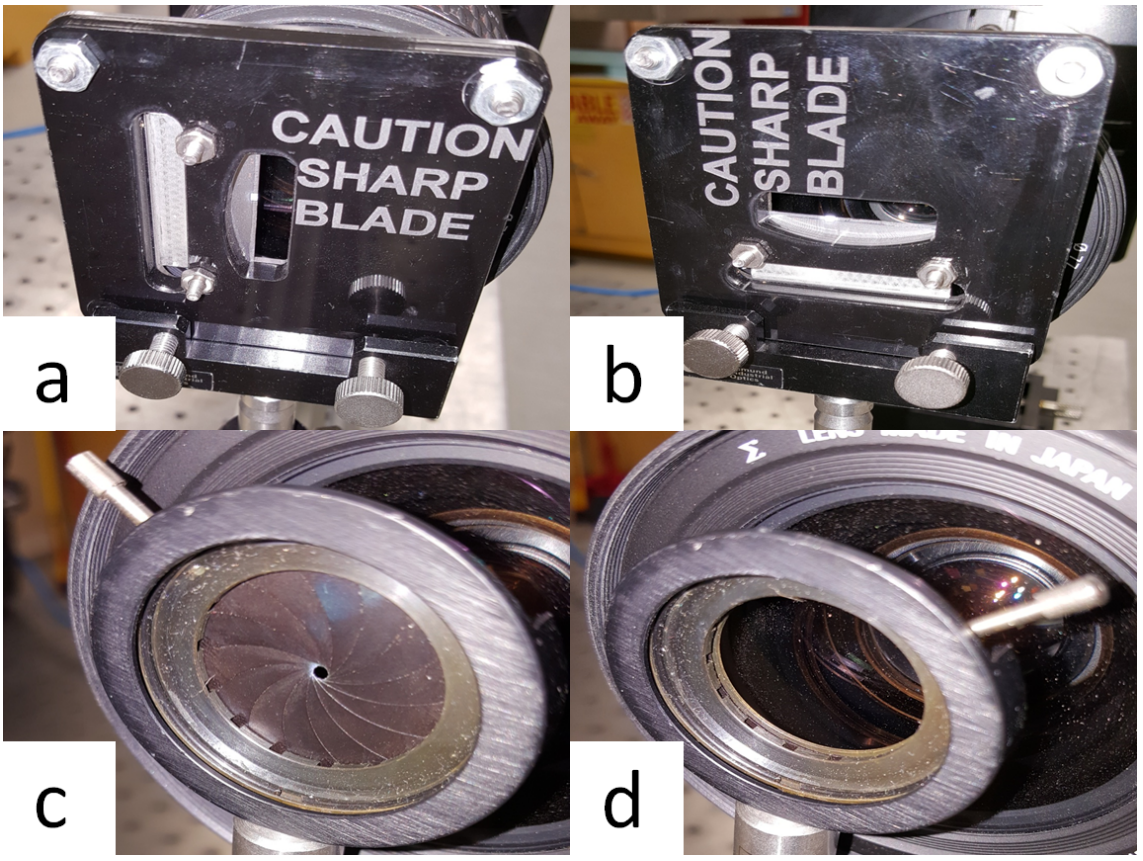

Figure 2.3: Images of the cutoff variations (a) vertical knife edge, (b) horizontal knife edge, (c) circular cutoff with a lever actuated iris diaphragm and (d) focused shadowgraph (no cutoff) with a fully opened lever actuated iris diaphragm.

The horizontal and vertical cutoff used were razor-blade knife edges. For the circular cutoff a lever actuated iris diaphragm was used, for focused shadowgraph the iris diaphragm was fully opened as shown in Figure 2.3.

2.2 Helium jet

For the subsonic test a helium jet with a straight exit section as shown in Figure 2.4 was used. The jet was operated with a helium gas cylinder and a pressure regulator to step down the operating pressure to 138 kPa. Helium gas was selected as the medium since it has the lowest density and provides the largest density gradient when compared to acetylene, air, argon methane, nitrogen and most readily available gases as shown on Table 2.2 [20]. The large density gradient of helium and provides a large change in the index of refraction and a large pixel intensity gradient in the schlieren images.

The schlieren image in Figure 2.5 produces sufficient turbulent features at steady state for good SIV analysis. During the initial transient state there was not sufficient turbulent features present as shown on Figure 2.5. The dark region on the left is the exit plane of the jet. Laminar flow is seen a short distance from the exit plane, but becomes turbulent as the distance increases from the exit plane.

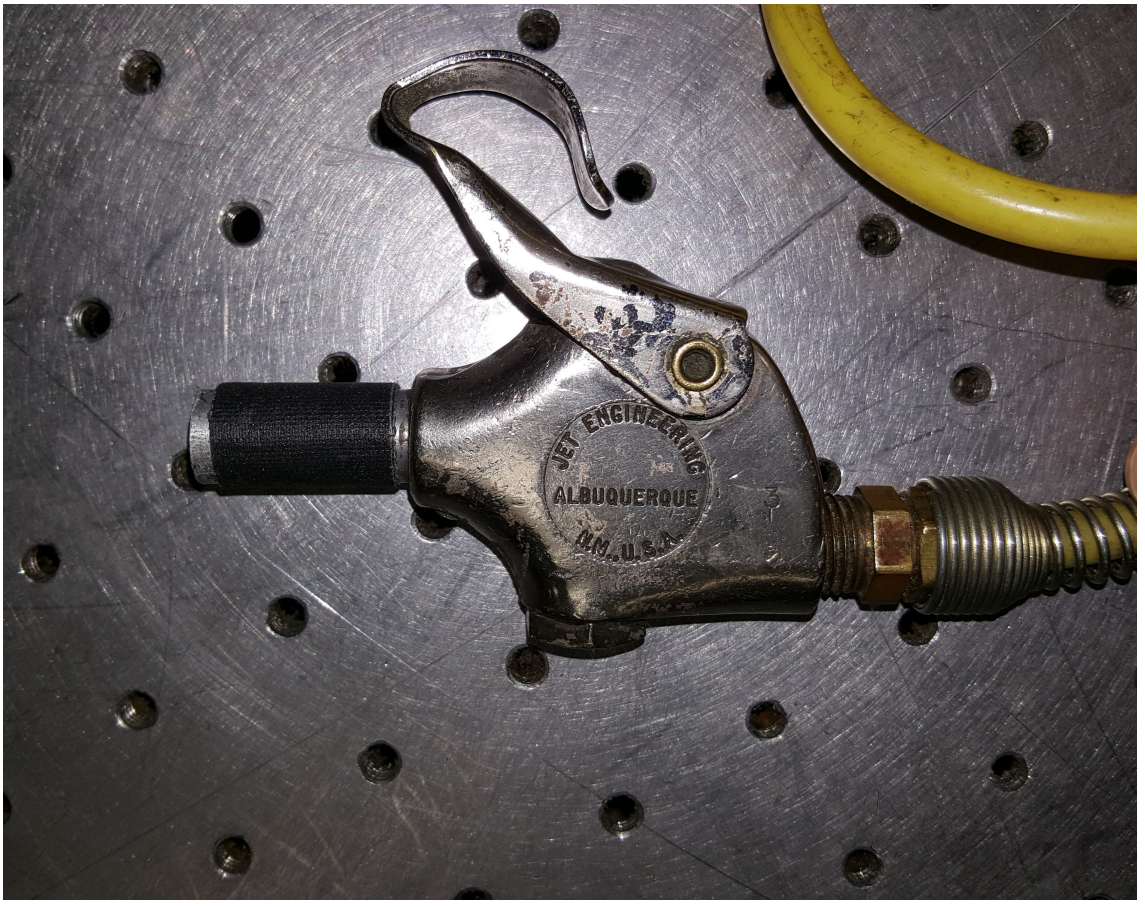

Figure 2.4: Helium jet apparatus.

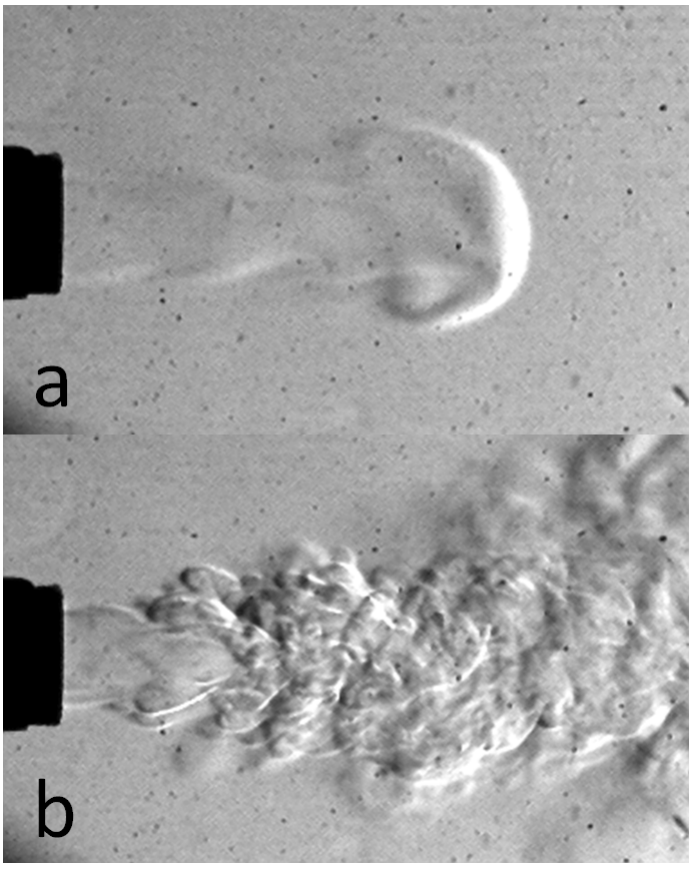

Figure 2.5: Raw schlieren image of the helium jet with a vertical knife edge as a cutoff at (a) initial transient state and (b) steady state.

Table 2.2: Density of various gases at normal temperature (20°C) and pressure (101 kPa).

Gas	Density (kg/m^3)
Acetylene	1.092
Air	1.205
Argon	1.661
Helium	0.166
Methane	0.668
Nitrogen	1.165

2.3 Micro-turbine

The mid-range velocity testbed was a JetCat P80-SE micro-turbine, which had an exit diameter of 102 mm and is shown in Figure 2.6. The JetCat P80-SE was operated with a fuel mixture of 95% kerosene and 5% turbine oil (part number: 61197-00) and produces a sub sonic exhaust plume. The disadvantage of using the micro-turbine is that it is intended for hobbyist use and not for research purposes. The on board data monitor only provided live data and did not have the necessary components to support a data acquisition system. Due to this condition, the micro turbine was tested at the maximum operating conditions as seen on Table 2.3 and the live data was read from the data monitor [21]. During testing all four cutoff were examined,: horizontal, vertical , circular and focused shadowgraph (no cutoff) as shown in Figure 2.7.

Table 2.3: Maximum operating conditions for the JetCat P80-SE as specified by the manufacturer.

Parameter	Values
Engine speed	125,000 RPM
Thrust	97 N
Fuel consumption	.0031 kg/s
Exit velocity	388 m/s
Power output	18.8 kW

The velocity of the micro-turbine exhaust could not be measured directly with a physical instrument or calculated with theoretical values to provide a reference for the SIV. Physical measurements such as the hot-wire anemometer or pitot tube could not be used without risking damage to the instruments. PIV was not suitable due to the difficulty in injecting seeding particles. Theoretical values could not be computed due to lack of data acquisition systems provided with the micro-turbine. Therefore, a reference exit velocity of 388 m/s was used for the maximum operating conditions, which was specified by the manufacture [21]. The maximum operating conditions were verified with the on board live data monitor.

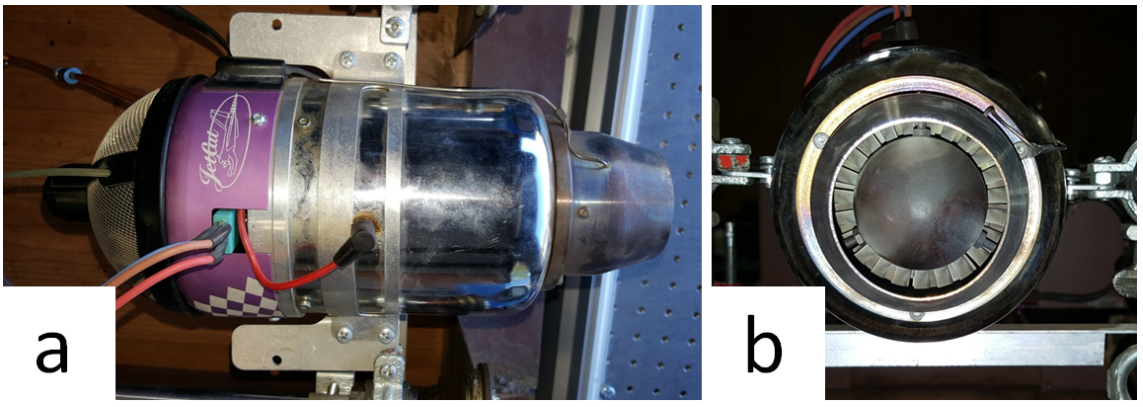

Figure 2.6: Overview of the JetCat P80-SE, (a) side view and (b) exhaust exit.

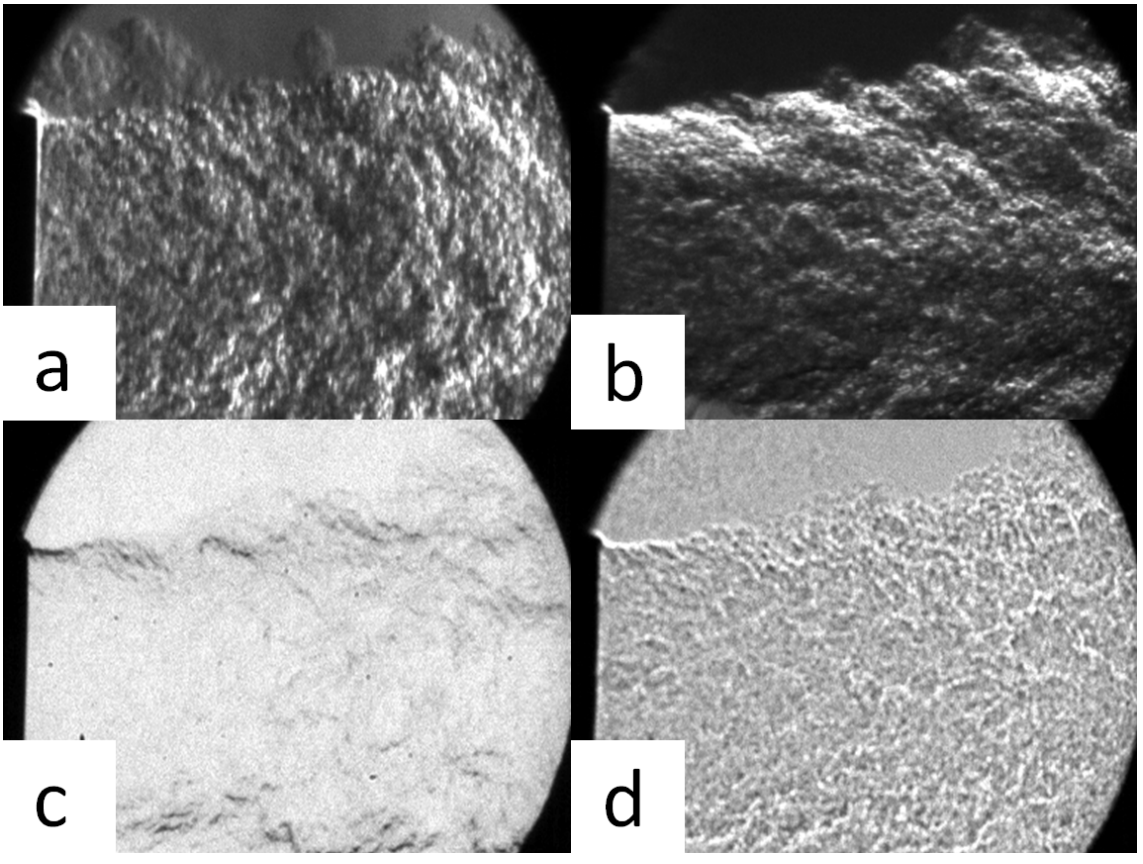

Figure 2.7: Schlieren image of the JetCat P80-SE using all cutoff variations: (a) vertical knife edge, (b) horizontal knife edge, (c) circular cutoff with a lever actuated iris diaphragm, and (d) focused shadowgraph (no cutoff).

2.4 Small-scale liquid rocket engine

For the supersonic velocity test, a small-scale liquid rocket engine exhaust was selected as shown Figure 2.8 a and b. The small-scale liquid rocket engine was designed with a nozzle exit area (A_e) to throat area (A^*) of $A_e/A^* = 9.97$ to produce a Mach 3 exit [22]. The rocket engine propellants are liquid ethanol (ETOH) and nitrous oxide (N2O). Experimental runs are limited to a 10 s run time and allow for a minimum of 1 s steady state condition. The engine is constructed of oxygen-free high thermal conductivity copper (OFHC) and 303 stainless steel and features a modular design that allows the possibility to test various injector, chamber and nozzle dimensions. Ignition of the propellant mixtures is provided via an automotive spark plug and a gaseous hydrogen and oxygen mixture. Data acquisition and system controls are supported via National Instruments (NI) hardware and NI LabVIEW software. Further details of the system are available in [22].

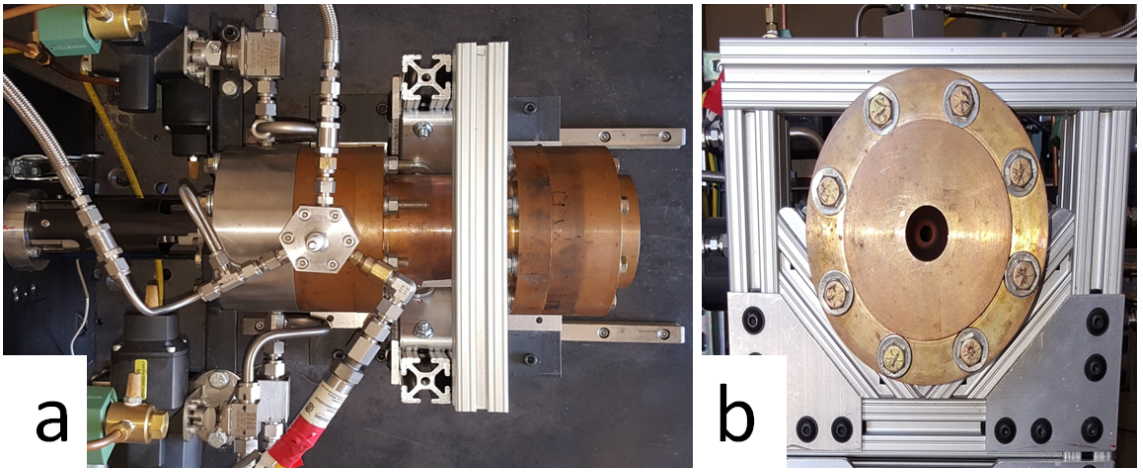

Figure 2.8: The small-scale liquid rocket engine (a) top view and (b) exhaust view.

For the small-scale liquid rocket engine two experimental data sets were selected, test 1 and test 2, which were performed on 03/21/2018 and on 05/02/2018, respectively. The experimental conditions for each run are shown in Table 2.4 and 2.5 and a subset of the processed run data are shown in Figure 2.9 and 2.10. The parameters from the experimental results are used as the input parameters to generate theoretical results using NASA chemical equilibrium with application (CEA) to compare results. NASA CEA is a program, which calculates theoretical rocket performance from the thermodynamic and transport properties of given propellants and oxidizer to fuel ratio (O/F) [23]. The primary parameter selected to evaluate the rocket performance during steady state is the specific impulse I_s, which is the thrust output per mass flow rate in [24]. In equation 2.1, I_s is the specific impulse, F is the thrust, $\dot{m}_{Total\ in}$ is the total mass flow rate in of the propellants and g_o is the gravity constant 9.81 m/s^2.

$$I_s = \frac{F}{\dot{m}_{Total\ in}\, g_o} \tag{2.1}$$

Table 2.4: Steady state test results from the rocket tests 1 and 2 performed on 03/21/2018 and 05/02/2018, respectively .

Parameters	Values	Values
Test	Test 1 (03/21/2018)	Test 2 (05/02/2018)
Start time	66 s	130.5 s
End time	70 s	131.5 s
O/F	4.52	3.83
ETOH pressure	7.99 MPa	8.64 MPa
ETOH temperature	291 K	294 K
N2O pressure	8.20 MPa	7.61 MPa
N2O temperature	289 K	291 K
P_c	6.26 MPa	5.98 MPa
$\dot{m}_{Total\ in}$	0.223 kg/s	0.203 kg/s
Thrust	491 N	450 N
I_s	224 s	226 s

Table 2.5: Theoretical test results from NASA CEA using steady state test results from the rocket tests 1 and 2 performed on 03/21/2018 and 05/02/2018, respectively.

Parameters	Values	Values
Test	Test 1 (03/21/2018)	Test 2 (05/02/2018)
O/F	4.52	3.83
P_c	6.26 MPa	5.98 MPa
$\dot{m}_{Total\ in}$	0.208 kg/s	0.198 kg/s
Thrust	535 N	503 N
MACH number	3.31	3.39
Exit velocity	2,577 m/s	2,535 m/s
I_s	262 s	258 s

The experimental tests with the small-scale liquid rocket engine had lower measured specific impulse than predicted with CEA as shown on Table 2.6. The

parameters that contributed to a lower experimental specific impulse were a higher total mass flow rate and lower thrust measurement than those values predicted by NASA CEA. The difference in the theoretical and experimental values are noted here for completeness, the thesis goals of measuring the exhaust plume, however are not hindered by the experimental errors. Future work on the rocket engine platform will investigate these differences.

For the rocket test only two of the cutoffs were tested, vertical and focused shadowgraph (no cutoff). Raw images from each imaging method are shown in Figure 2.11.

Table 2.6: Experimetnal error with respect to the theoretical values for tests.

Parameters	Value	Value
Test	Test 1 (03/21/2018)	Test 2 (05/02/2018)
$\dot{m}_{Total\ in}$ error	7.21 %	2.53 %
Thrust error	8.22 %	10.53 %
I_s error	14.5 %	12.4 %

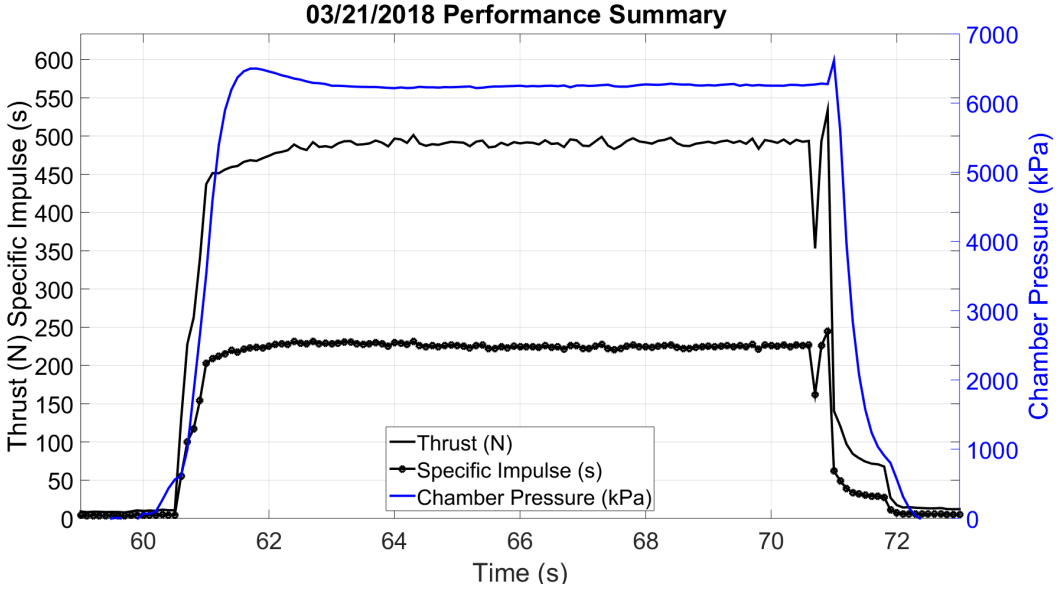

Figure 2.9: Overall performance summary for the rocket test 1 performed on 03/21/2018 with an O/F = 4.52.

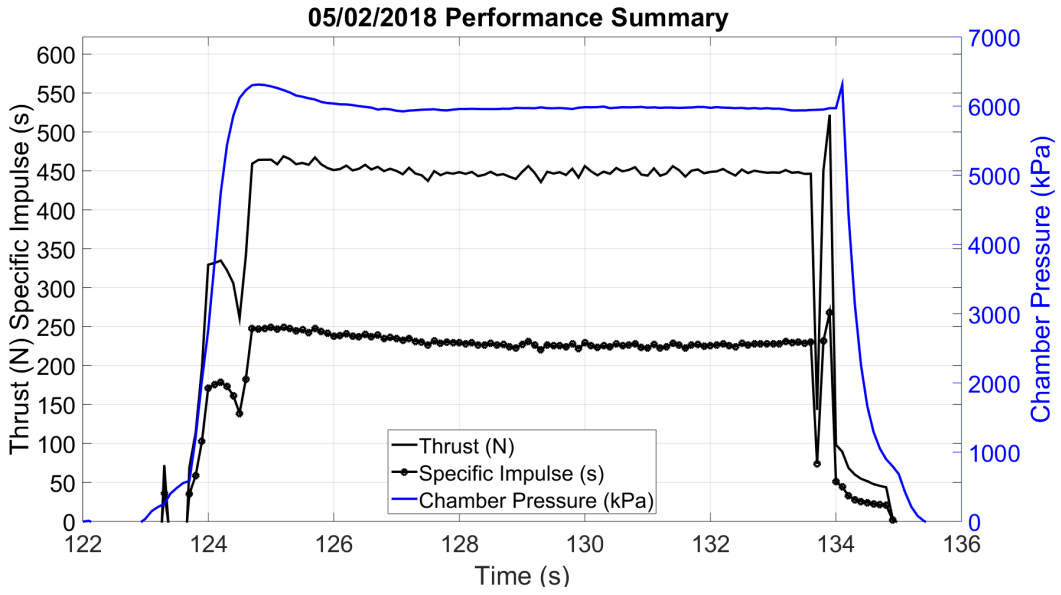

Figure 2.10: Overall performance summary for the rocket test 2 performed on 03/21/2018 with an O/F = 3.83.

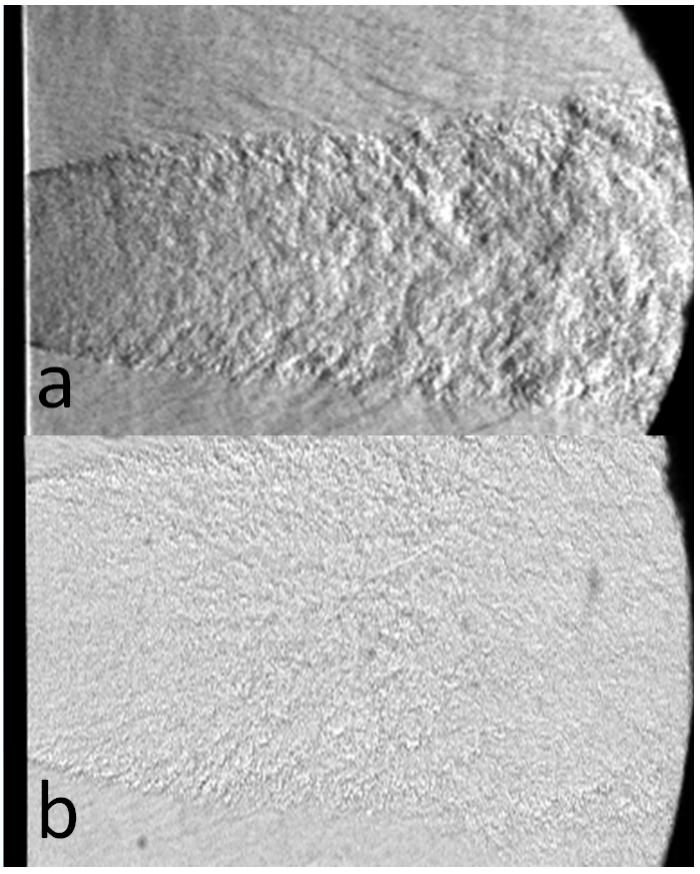

Figure 2.11: Schlieren images of the small-scale liquid rocket engine tests using (a) a vertical knife edge as a cutoff (test 1) and (b) focused shadowgraph using no cutoff (test 2).

CHAPTER 3

IMAGE PROCESSING

3.1 Introduction

The schlieren images were recorded in 8 bit gray scale using a monochrome camera, which provides 256 levels of pixel intensities. The pixel intensity gradient visualized in a schlieren image is due to the refracted light as it passed through the various densities of the medium. The gray intensity region is difficult to isolate from the objects of interest, since a large portion of the image is the gray region. The intermittent appearance and overlapping of the features causes obscure, instead of well-defined, edges. Although there are regions of excessive noise in the images, the turbulent features are distinguished by the lighter and darker intensity regions as shown in Figure 3.1 a. Since the light in a schlieren image is either blocked by the cutoff or directed towards the camera, an approach was developed here to isolate the dark and light turbulent features with image processing methods.

3.2 Background subtraction

To separate the turbulent features of interest from the image and to reduce the signal to noise ratio, image pre-processing techniques are applied before the correlation methods were applied. A subtraction eliminates the noisy regions due to electronic components such as shading calibration or imperfections in the optical equipment and results in images that enhance the appearance of the turbulent features. Background subtraction is performed by subtracting a common image in one of two methods: with a tare image that is taken before the test or by generating one with the images in the data set.

For the first background subtraction method the tare image removes similar pixel intensities from all the images in the data set to reduce the noise. The test image is shown in Figure 3.1 and when the tare image in Figure 3.2 a is subtracted from the test image, the new image must have a pixel intensity value between 0 to 255. During the subtraction process the absolute value of the difference is used to create a new image. This prevents a loss of data by preventing negative pixel values as shown in Figure 3.2 c, where 0 is black and 1 is white.

The second method is to create a tare image from the data set with additional step to address the zero values in an image. The first step in this process is to average each pixel intensity at its location for the entire data set and then to normalize the pixel intensity by using the bit depth to create an average flow image, which is used as a tare image as shown on Figure 3.3 a. The histogram is computed and the range of pixel intensities is limited to the maximum and minimum intensities of the data set. A median pixel intensity is also computed using the newly defined range and is added to each pixel of the image. With this method the zero values are replaced with the new mid value and remove the black regions of the image. This will eliminate those sections that are blocked off by components or outside the parabolic lenses as shown on Figure 3.3 c. In addition a contrast adjustment was applied to enhance the visibility of the dark and light turbulent features. A contrast adjustment was applied since the objects of interest are towards the lighter and darker pixel intensities. This helps to better define and eliminate the blurred edges of the turbulent features as shown in Figure 3.4 a.

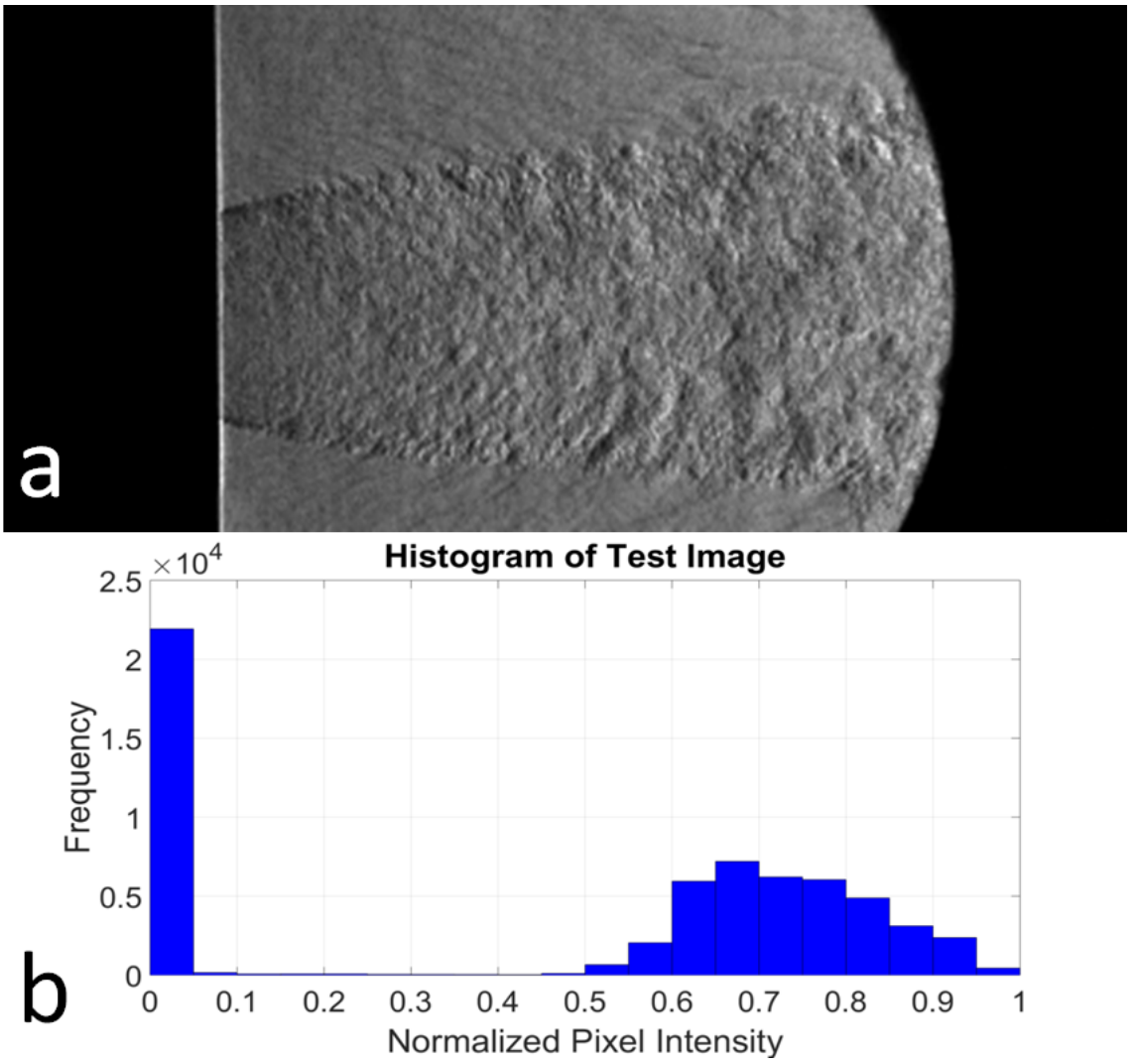

Figure 3.1: (a) Raw schlieren image of the rocket test 1 performed on 03/21/2018 and the (b) histogram of the normalized pixel intensities.

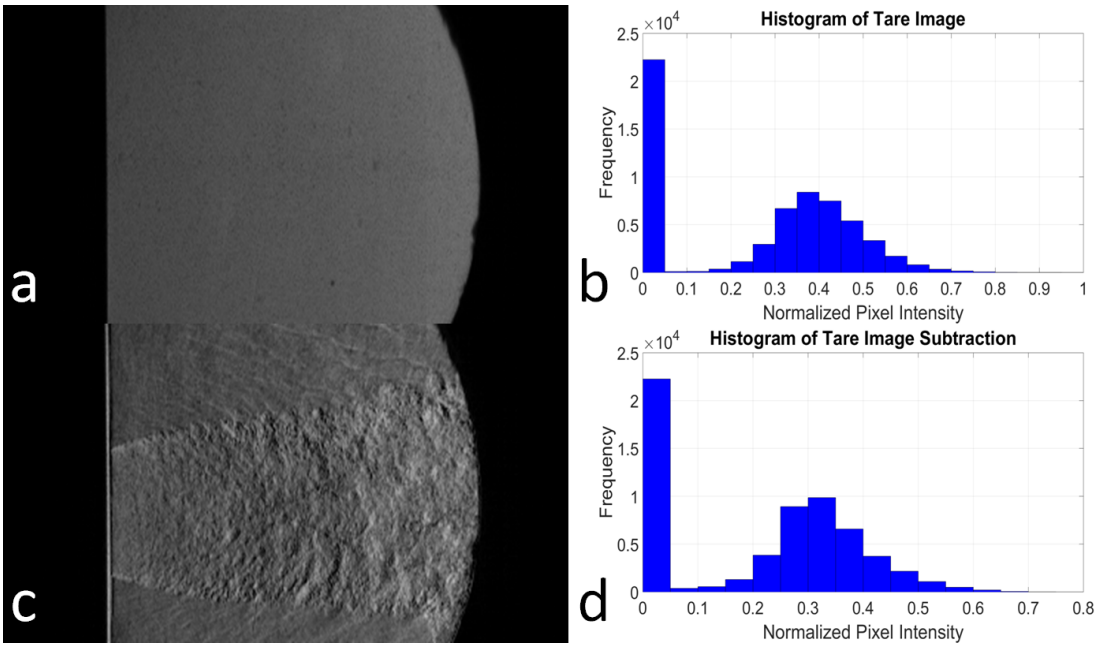

Figure 3.2: (a) Raw schlieren tare image of the rocket test 1 and the (b) histogram of the normalized pixel intensities. (c) Flow image after image subtraction and the (d) histogram of the normalized pixel intensities.

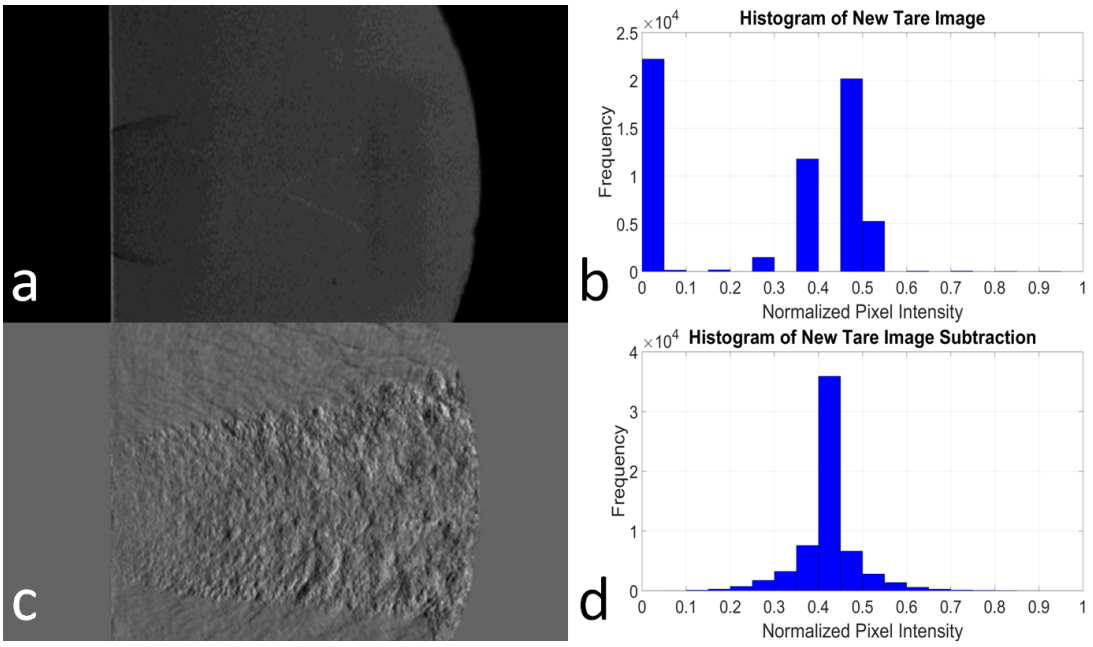

Figure 3.3: (a) Schlieren tare image of the rocket test 1 created from individual flow images and the (b) histogram of the normalized pixel intensities. (c) New flow image after image subtraction and the (d) histogram of the normalized pixel intensities.

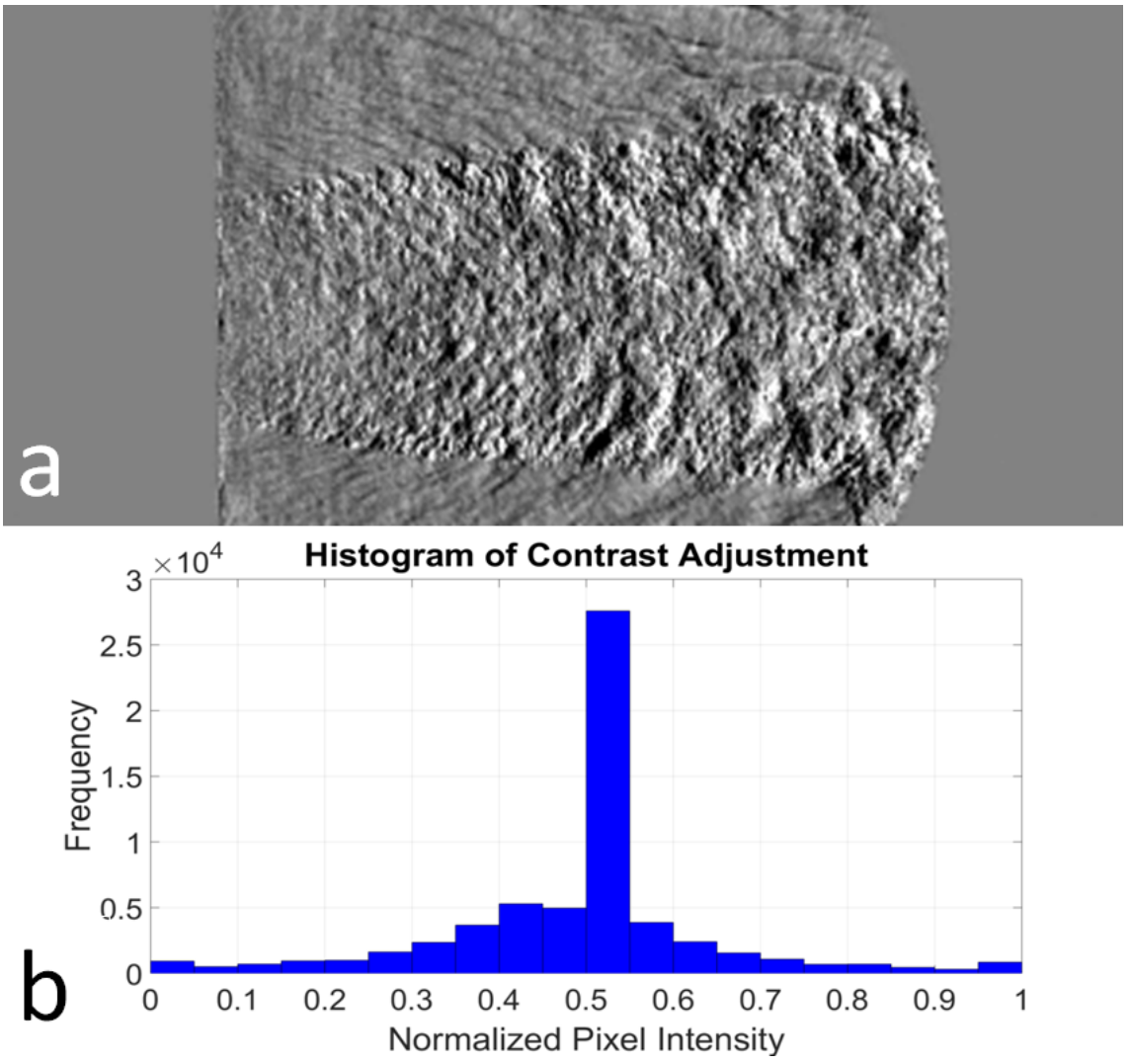

Figure 3.4: (a) Flow image after image subtraction with contrast adjustment of the rocket test 1 and the (b) histogram of the normalized pixel intensities.

3.3 Object identification

To facilitate the identification of the turbulent features of interest a multi-level threshold is applied. This is performed with the histogram of the pixel intensities of each image separated into three regions using a method developed by Nobuyuki Otsu [25]. This, multi-level threshold allows for the segmentation of the lighter and darker intensity turbulent features from the gray regions, whereas a single level threshold visualizes half of the features [26]. Once the multi-level threshold is applied, an image with three pixel intensities is returned. A threshold level of 1 is assigned a pixel intensity of 1 (black), between level 1 and 2 is assigned a pixel intensity of 128 (gray) and a threshold level of 3 is assigned a

pixel intensity value of 255 (white). This threshold allows for the visualization and isolation of the features from the background as shown in Figure 3.5 a.

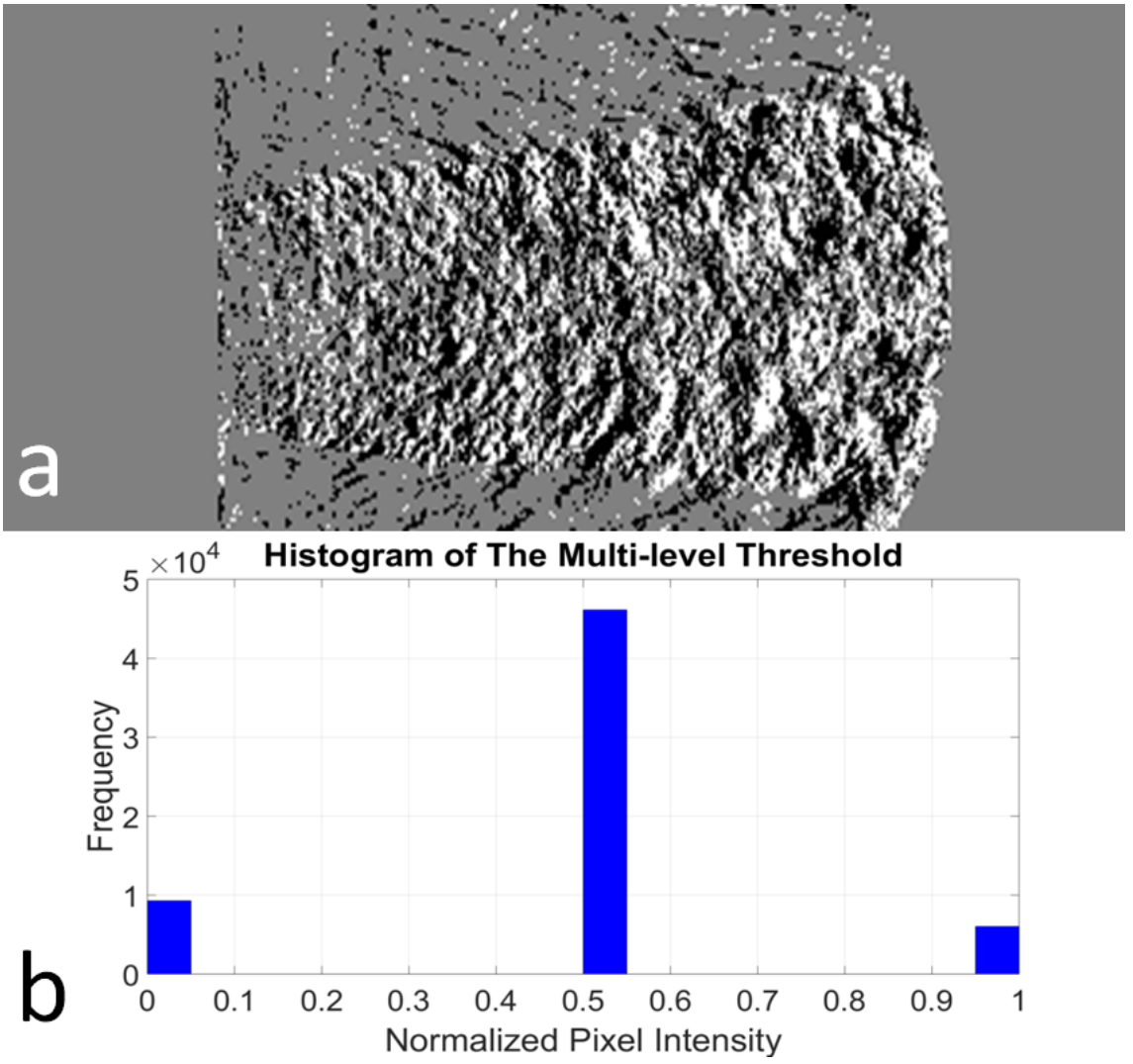

Figure 3.5: (a) Multi-level threshold applied to the rocket test 1 after tare image subtraction with contrast adjustment and the (b) histogram of the normalized pixel intensities.

Once the turbulent features can be clearly identified their properties including the size, shape, location and centroid can be calculated using the MATLAB function *Regionprops*. The process to identify the properties requires the conversion from a gray scale images into a binary images as shown in Figure 3.6, for the segmentation of the turbulent features from the background [26]. The end result is two pairs of images one with black features, Figure 3.7 a and another with white features, Figure 3.7 c. If both are analyzed simultaneously the fea-

tures making contact are combined and result in overall decreased features count with an increased area as shown in Figure 3.8 b. If the turbulent features are separated the size distribution changes, while the number of smaller features increase the area of the features decrease as shown in Figure 3.8 c.

Using the identified properties a new image can be generated to isolate the features based on specified parameters, such as a size filter as shown in Figure 3.9. This allows for improved processing speed by directing the focus on specific turbulent features rather than the entire features of the image, limiting the noisy regions. Smaller features are desirable like those of PIV particles, since the window size would have a tighter fit around the feature, a larger search window may enclose parts of other features and decrease correlation [12].

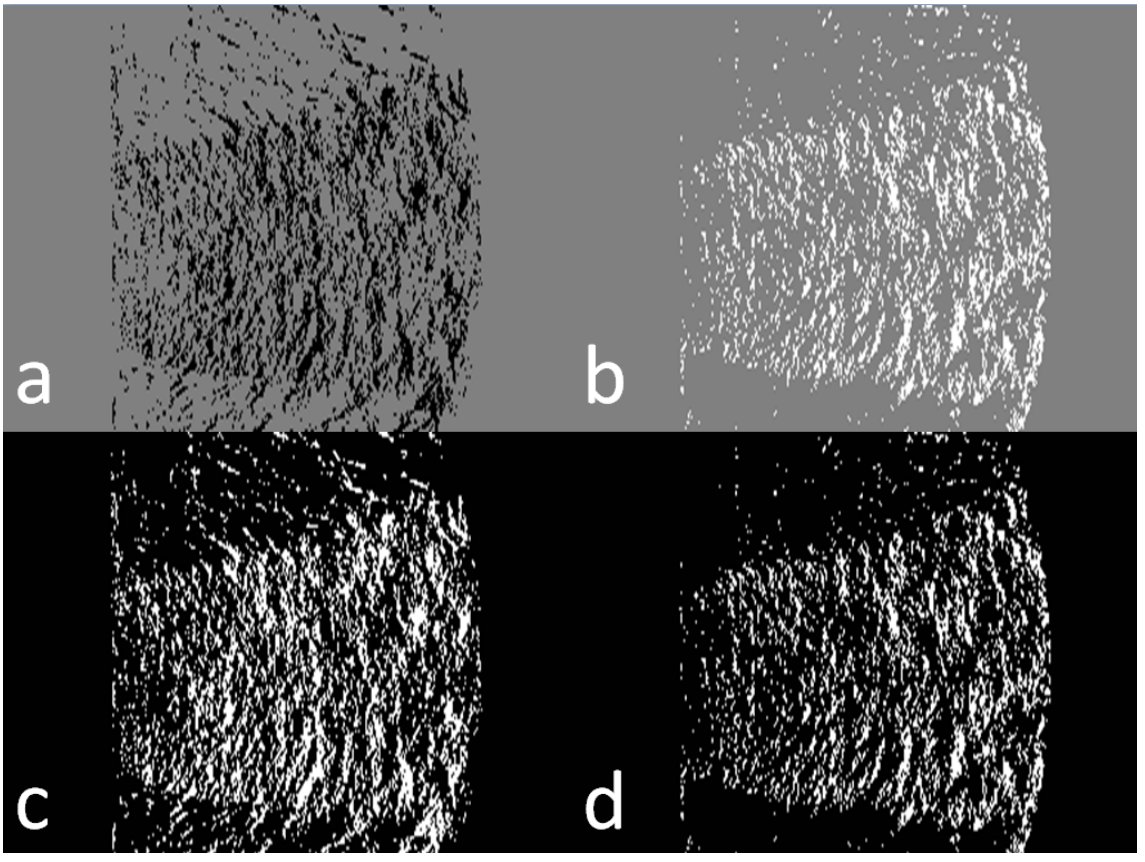

Figure 3.6: The (a) black and (b) white turbulent features separated with the binary conversion of the (c) black and (d) white features.

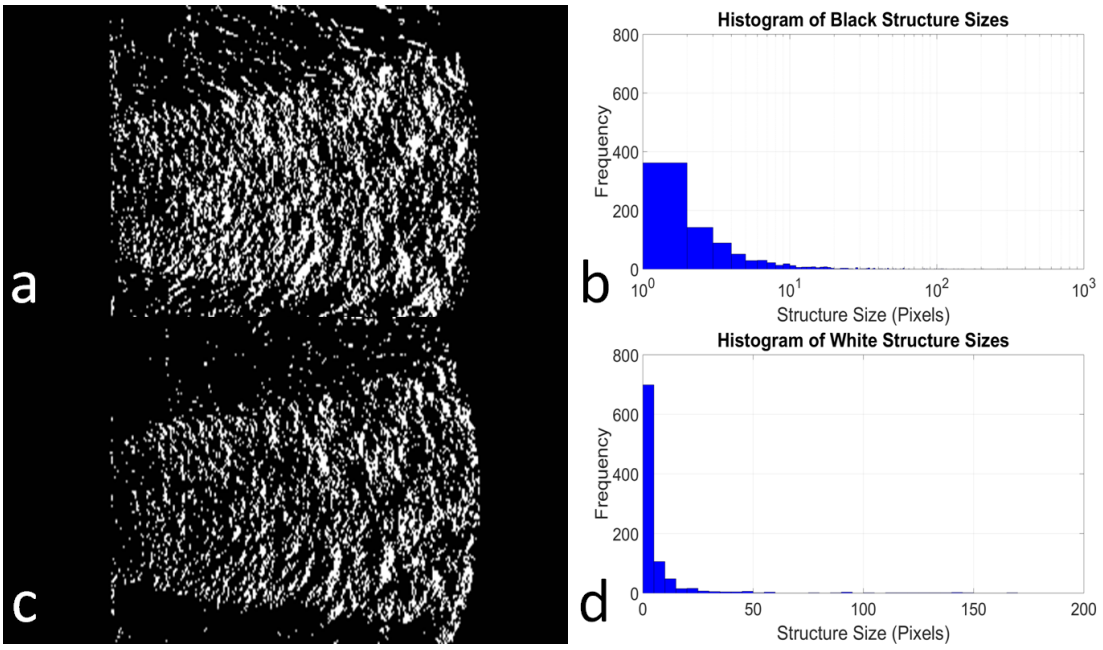

Figure 3.7: (a) Reconstructed image with just the black turbulent features from Figure 3.5 and the (b) size distribution of the black turbulent features. (c) Reconstructed image with just the white turbulent features from Figure 3.5 and the (d) size distribution of the white turbulent features.

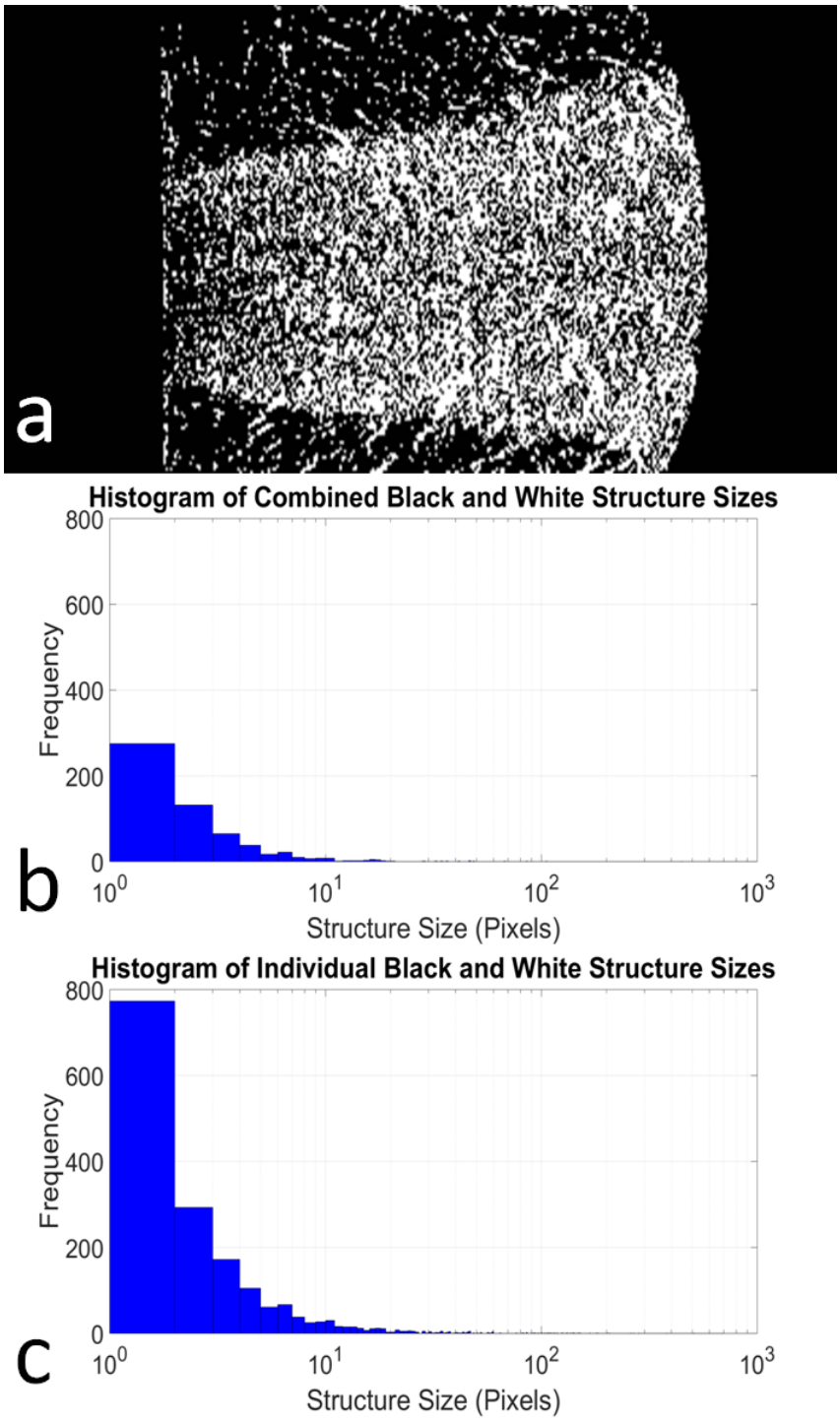

Figure 3.8: (a) Reconstructed image with the black and white turbulent features combined from Figure 3.5, with histograms of unequal bin numbers and widths. (b) The size distribution of the black and white turbulent features combined and the (c) size distribution of the individual black and white turbulent features.

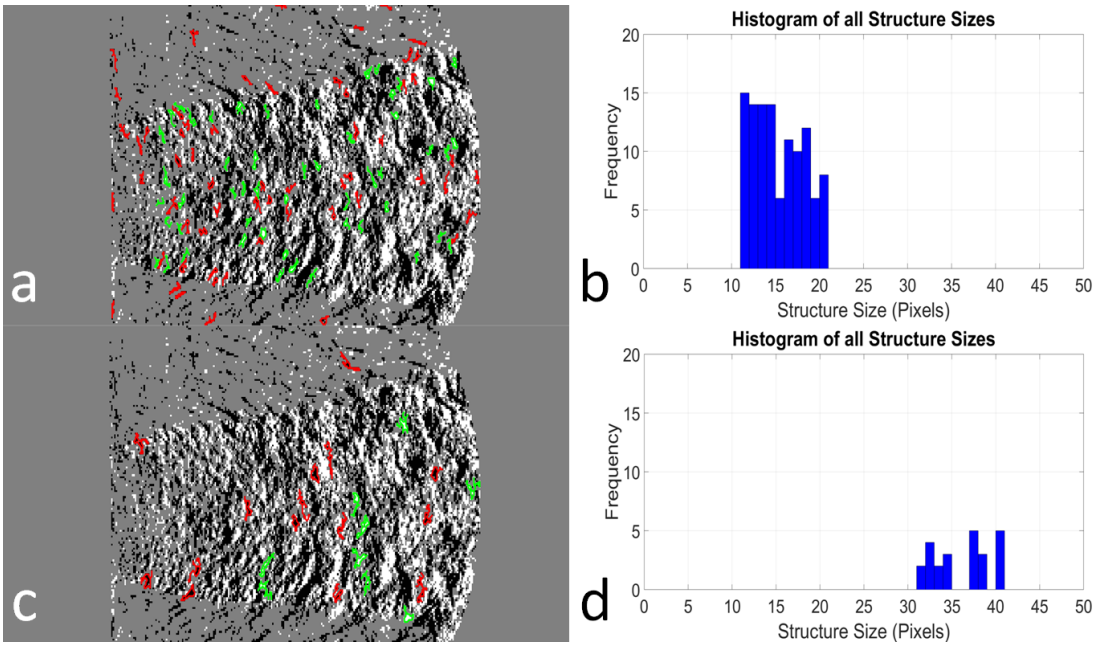

Figure 3.9: (a) Reconstructed image with the black (red outline) and white (green outline) turbulent features with a filter size of 11-21 pixels applied to highlighted features and (b) the size distribution histogram. (c) The reconstructed image with a size filter of 31-41 pixels applied to highlighted features and (d) the size distribution histogram.

3.4 Object tracking

Traditional seeding particles like those in PIV are small and uniform in size, they are also of similar intensities when they are illuminated as shown in Figure 3.10 a. In SIV turbulent features are classified here as one of two different intensities and are of various sizes and shapes as shown in Figure 3.10 b. The variations in turbulent features make it difficult to set a fixed interrogation window to track particles like those in PIV software. A Lagrangian tracking approach is applied here to track individual features through time, due to the size and shape variations of the turbulent features.

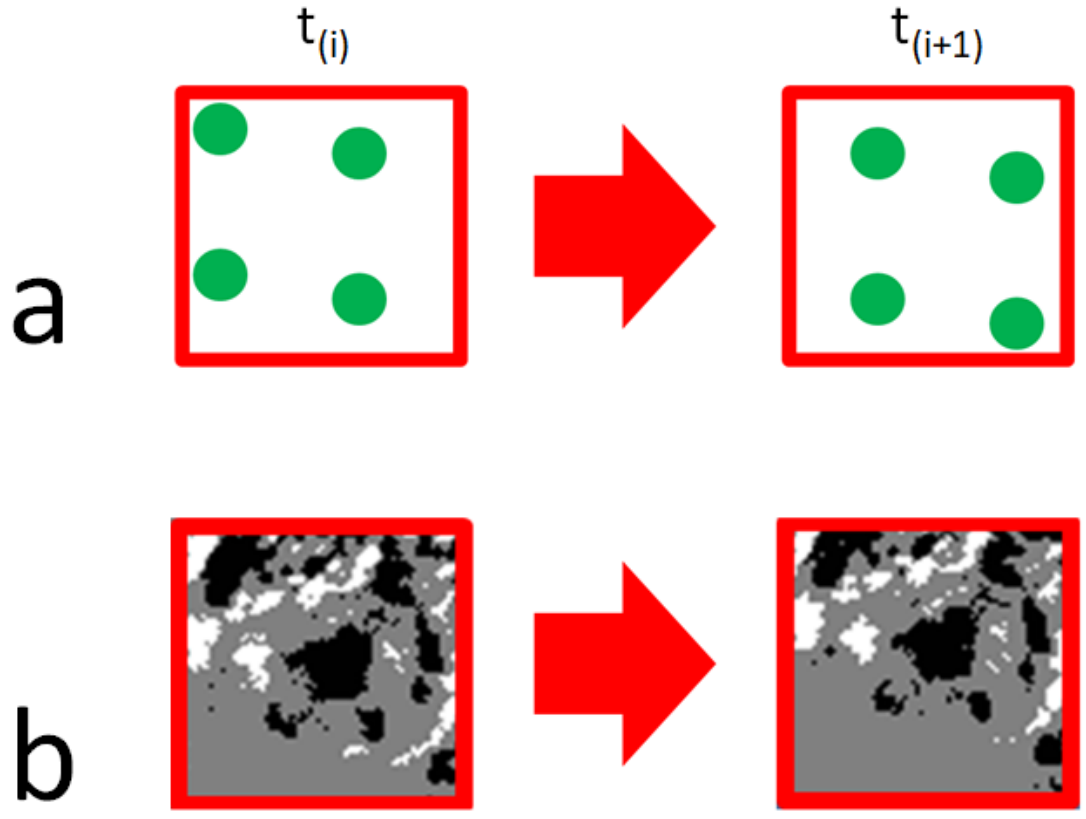

Figure 3.10: A comparison of (a) the seeding particles in PIV and (b) turbulent features in SIV.

A challenge in tracking turbulent features is the natural chaotic behavior and their intermittent appearance, which is compounded by the 2D path average in the schlieren image across the axisymmetric flow of the testbed. Given adequate temporal resolution the coherent turbulent features will retain their shape between frames to calculate a motion path and velocity. Incoherent turbulent features will not be addressed due to their intermittent appearance and rapid deformation. The tracking of objects that deform in linear, shear and rotational manners as shown in Figure 3.11 can be performed, but this will require additional pattern recognition algorithms and programming needs outside the scope of this research [3]. Other studies have identified more detailed recognition algorithms, including those proposed by Tokumaru and Dimotakis [27].

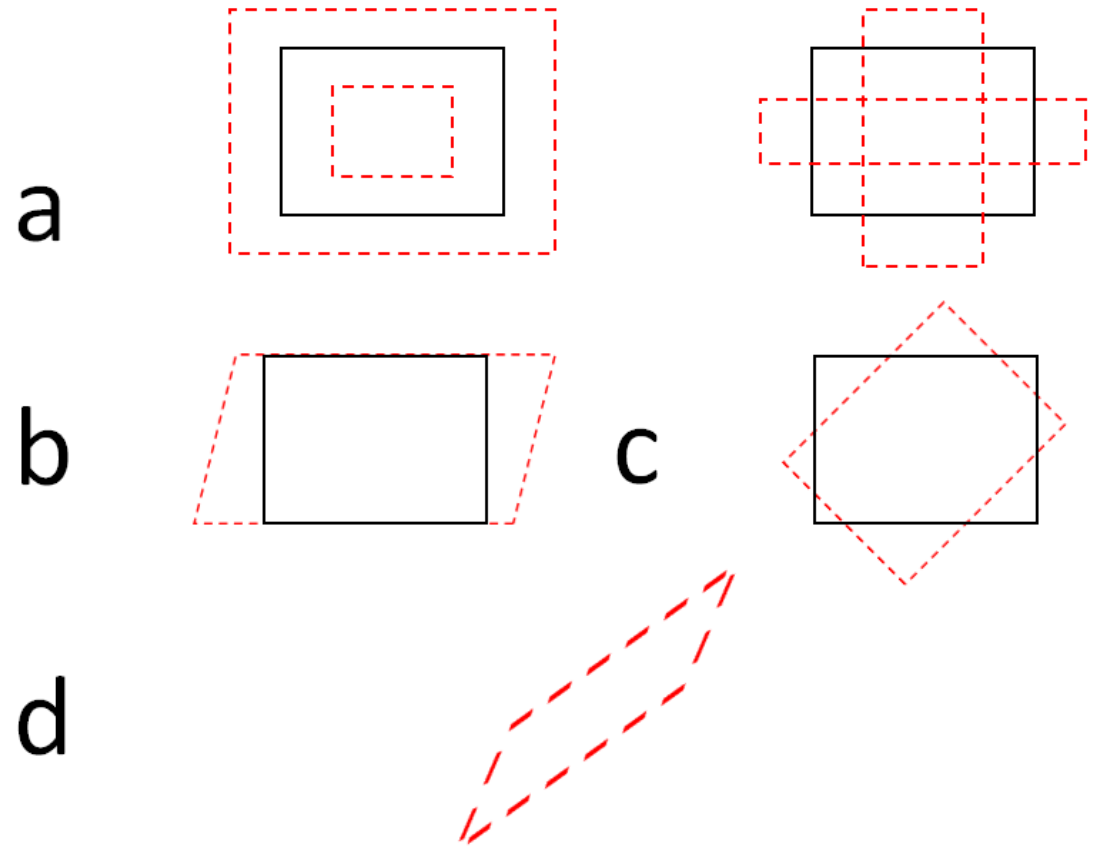

Figure 3.11: Forms of turbulent feature deformation (a) linear (b) shear (c)rotational (d) simultaneous deformation.

3.5 Reference position

Once the turbulent features have been separated from the background, identified, and isolated, the next process is to determine a method to calculate the reference position for each turbulent feature. The turbulent features are deforming and the leading edge is not consistent, thus the true displacement is affected. Therefore the location of the turbulent feature will be based here on the centroid to account for the various forms of deformation, an example of the turbulent feature deformation and centroid in Figure 3.12. By using the centroid as the reference point it provides coordinates at a sub-pixel level and in turn sub-pixel displacement.

Even with the sub-pixel centroid locations, the uncertainty is quantified as ± 1 pixel, due to the limitations in the image resolution. The major contribution to this uncertainty is the threshold application to the image during the conversion

from gray scale to binary. This is due to the effects on turbulent features as they may increase or decrease in size and influence the calculation of the centroid. The uncertainty could be reduced by systematically examining the effect of different thresholding processes on the turbulent feature's centroids, but this is highly dependent on the schlieren imaging itself and is outside of the scope of the present work.

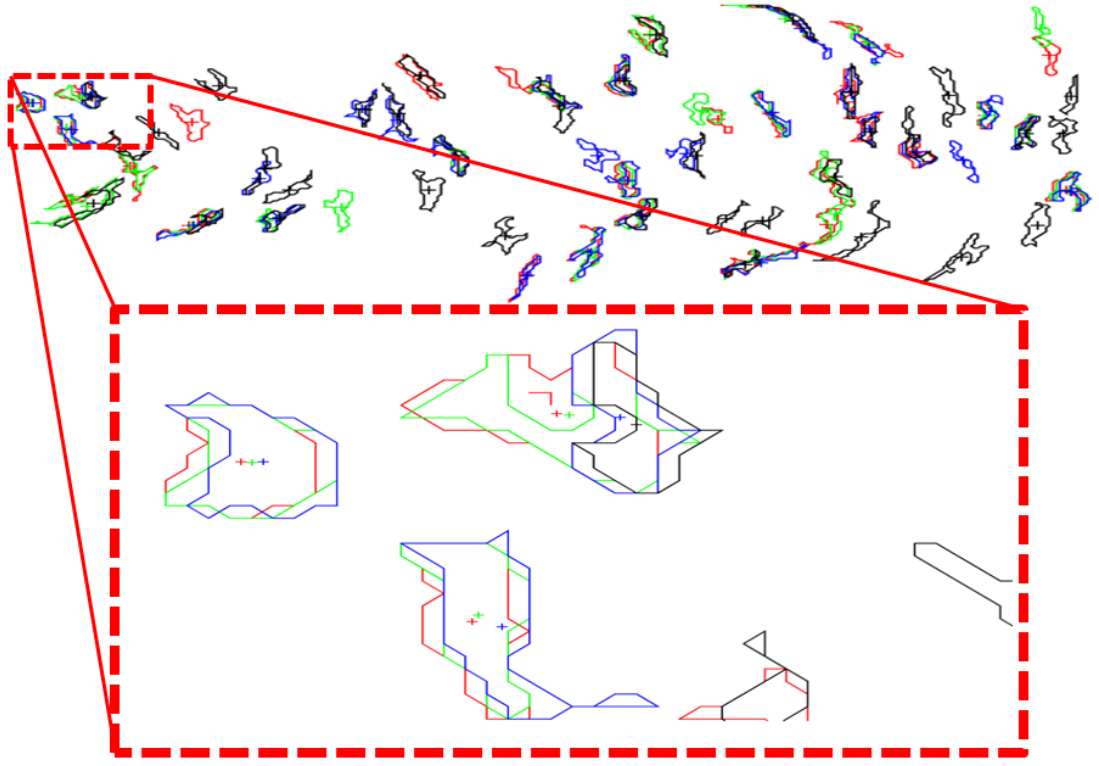

Figure 3.12: Reconstructed image with 4 frames superimposed in colors red, green, blue and black in order of increasing time to demonstrate the motion of centroids (+) and deformation of the turbulent features (outline).

3.6 Path construction

Once the turbulent features have been identified and tracked, their paths can be constructed. The path construction can be performed by grouping turbulent features with similar features within the same area as shown in Figure 3.13. The minimum Euclidean distance is computed to form the path of the turbulent feature [26]. By computing the positive displacement of the turbulent feature the incoming and overlapping features can be dismissed and decrease the possibility of poor path construction. By capturing the entire flow field, localized measurements can be isolated by restricting the field of view to a certain location. The

identification and isolation of the high and low velocity regions can be used to evaluate the flow characteristics of the flow. This will allow for the analysis and differentiation of the shear layer and center velocity of the flow.

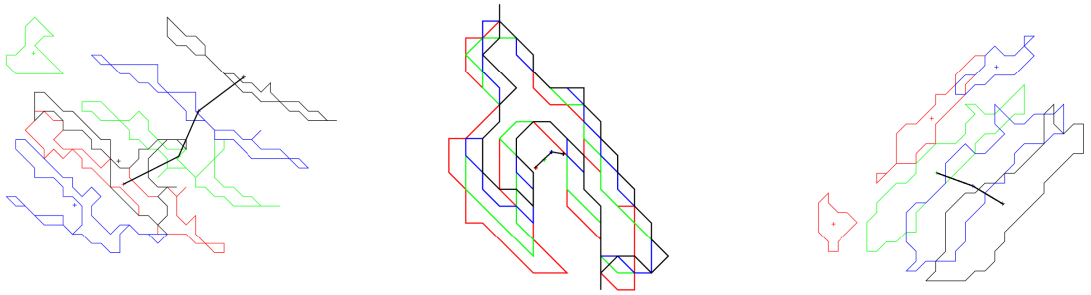

Figure 3.13: Path construction example of centroids with matching turbulent features, were the frame sequence is red, green, blue and black.

CHAPTER 4

VELOCITY MEASUREMENTS

Each data set from each testbed was separated into four, equally-sized large regions of interest at different axial distances from the exit plane. Measurements of turbulent feature sizes and velocities are presented in these regions of the exhaust flows. The color sequence used for regions of interest are: red (region 1), green (region 2), blue (region 3) and black (region 4) as shown on Figure 4.1. Manual turbulent feature tracking was performed with the settings as shown in Table 4.1 for the regions of interests of each data set. An area filter was applied to suppress the turbulent features that were excessively small or large to prevent over-congestion of the turbulent features within the region of interest.

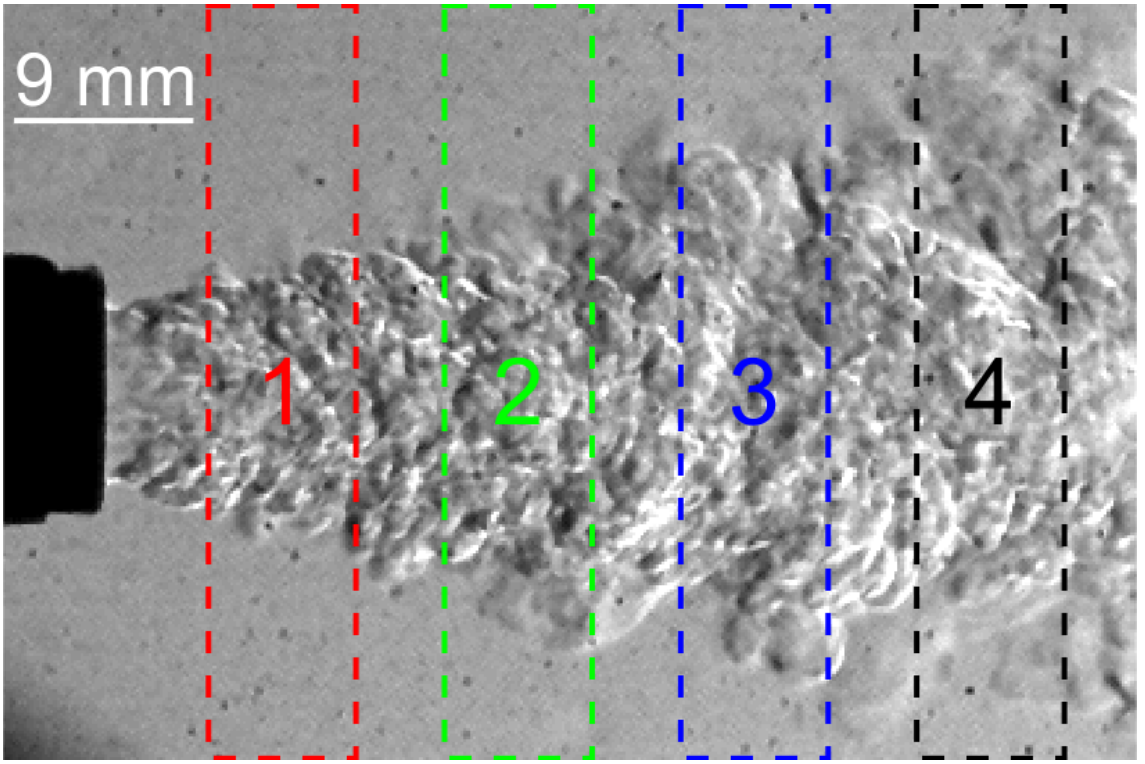

Figure 4.1: Schlieren image of the helium jet showing the 4 regions of interest and color code.

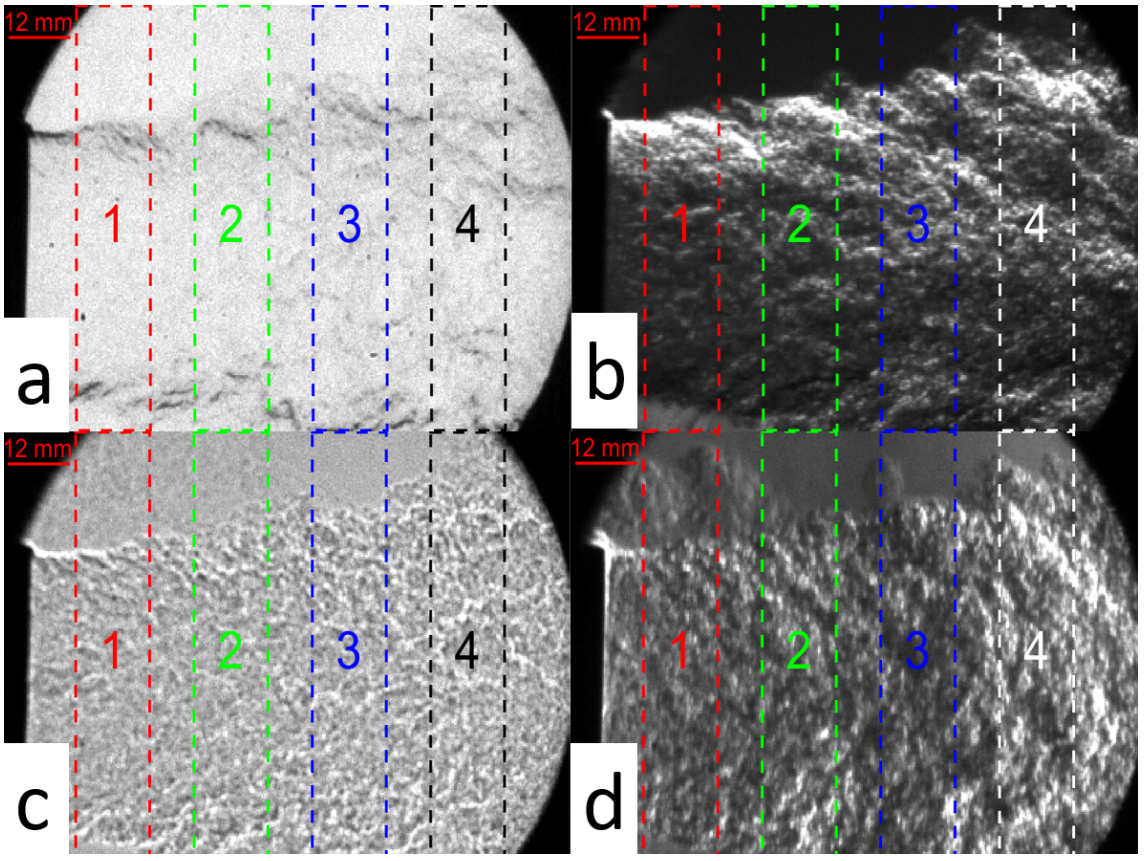

Figure 4.2: Schlieren images with cutoff variations used for the JetCat P80-SE with the 4 regions of interest and color code overlaid for the: (a) circular, (b) horizontal (c) focused shadowgraph (no cutoff) and (d) vertical cutoff.

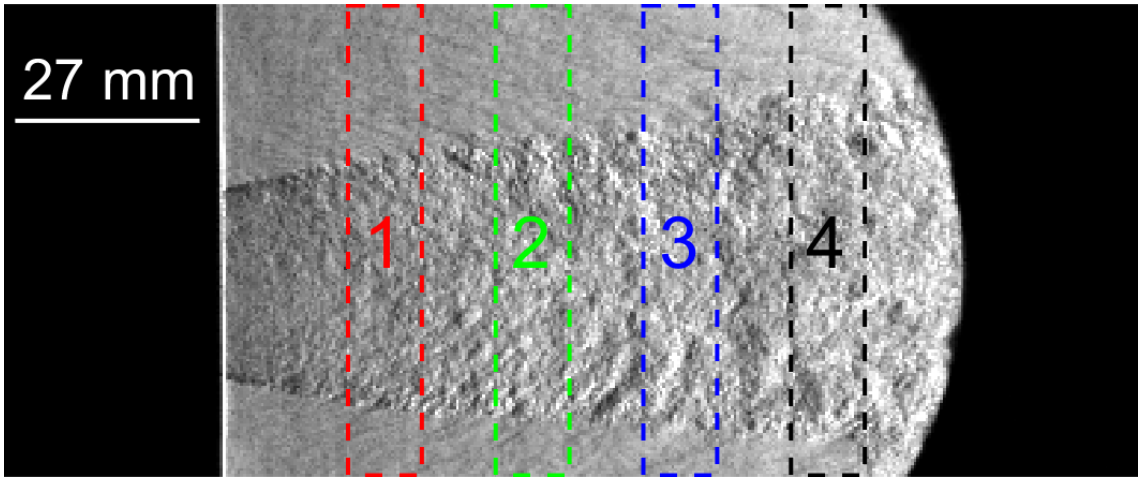

Figure 4.3: Schlieren image of the small-scale liquid rocket engine test 1 with a vertical cutoff, with the 4 regions of interest and color code shown.

Table 4.1: Regions of interest, filter size and scale for each data set.

Test	Region of Interest (pixels)	Particle Filter (pixels^2)	Image resolution (μm/pixel)
Helium jet	50x255	50 to 500	153.7
Micro-turbine circular cutoff	50x255	50 to 500	300.7
Micro-turbine horizontal cutoff	50x255	50 to 500	300.7
Micro-turbine shadowgraph	50x255	50 to 500	300.7
Micro-turbine vertical cutoff	50x255	50 to 500	300.7
Small-scale liquid rocket engine	25x159	25 to 75	444.1

The velocity measurements taken here were gathered by manually tracking the displacement of the turbulent features as they transition from one frame to the next. Each data set was separated into two sets, one for the black turbulent features and another for the white turbulent features. The color sequence used was red (frame 1), green (frame 2), blue (frame 3) and black (frame 4). Four frames were selected at a time to prevent the turbulent features from congesting the area and the colors red, green, blue, and black were selected on a white background compared to other color schemes.

The centroid was used to track the position of each turbulent feature. Once a matching turbulent feature was visually identified the centroid was selected and recorded until the turbulent feature no longer matched or it disappeared. The turbulent feature's centroid was only selected if it was subsequently found across the 4 frames.

The displacement was computed using the x and y coordinates of the turbulent feature's centroid. Where the initial position of the centroid is defined as (x_i, y_i) and the subsequent position is defined as $(x_{(i+1)}, y_{(i+1)})$. The Euclidean distance D_{xy} is calculated using a subsequent pair of centroids:

$$D_{xy} = \sqrt{(x_{(i+1)} - x_i)^2 + (y_{(i+1)} - y_i)^2} \tag{4.1}$$

The velocity is then obtained with the time separation of the frames. The velocity is averaged over the number of frames the turbulent feature was found to match.

The matching matching features were sorted into the regions of interest with the following 2 conditions:

- Condition 1, if a turbulent feature was found to be in contact with the outer bounds of a region of interest it was counted in that region.
- Condition 2, if a turbulent feature was found to be in contact with two regions it was counted in the first region it made contact in, going from left to right.

Forty velocity measurements were obtain per region of interest for each data set of images. This was done to provide a sufficient sample size, a normally distributed data set or a minimum of thirty samples are needed, due to the central limit theorem [28, 29].Twenty velocity measurements for each black and white turbulent features, which resulted in one-hundred and sixty velocity measurements per data set.

To compare the velocity measurements within the flow, the velocity measurements were normalized by the local region maximum and a histogram was made with a fitted gamma distribution. To compare all regions ten bins of equal widths were used to prevent unequal bin width due to the maximum and minimum values in each region.

4.1 Monte Carlo simulation of a free air jet

Due to the limited methods available to directly measure the velocity profile in each of the flows, an ideal velocity profile was constructed using a Monte Carlo simulation and data published by Fellouah et al [30]. The data published by Fellouah et al. was the velocity distribution of a free air jet at various distances downstream of the exhaust, measured using a hot-wire anemometer rake. The data set was digitized and a 6^{dth} order polynomial was fitted to obtain a function for the velocity profile at various radial and axial distances from the exit plane. The Monte Carlo simulation was chosen as it has been used by the scientific community to solve problems when insufficient data is available to resolve a smoothly varying phenomena [31]. Here the Monte Carlo simulation was applied using 100,000 randomly and uniformly generated points within a 3x3 unit square as shown in Figure 4.4 a. The radial distance for each point was calculated from the center then translated to the functions fitted to the velocity profiles as shown on Figure 4.4 b. Histograms were then generated from the digitized velocity profiles to show the distribution of velocities across the jets at different downstream locations. This histogram approach is used here to compare the manually measured data to theoretical histogram distributions generated from the Monte Carlo simulation.

The histogram of the velocity profile at each radial distance from the exit plane was plotted and fitted with a gamma distribution curve to determine trends as shown in Figure 4.5. In the data x is the axial distance from the exit plane,r is the radius, D is the diameter of the jet exit, u is the velocity and U is the maximum local velocity, this was the non-dimensionalization for the distance from a jet exit [30]. As the axial distance increases the histograms are skewed to the left where the lower velocities are present as shown in Figure 4.5. As the axial distance increases the the leading edge of the velocity profile becomes more Gaussian and the jet width begins to widen as shown in Figure 4.4 b. As the axial distances increases the velocity histograms are skewed to the left, where the lower velocities are present.The fitted curves are not only shifted to the left but the peakedness also increase downstream of the exit plane shown in Figure 4.6.

The transition from high to low velocity happens immediately as the shift can be seen from x/D=1 to x/D=2 as shown in Figure 4.6. This is due to the uniform core flow, which has not decayed due to the mixing of the shear layer, because of this x/D=1 has been omitted from the comparison of all testbeds.

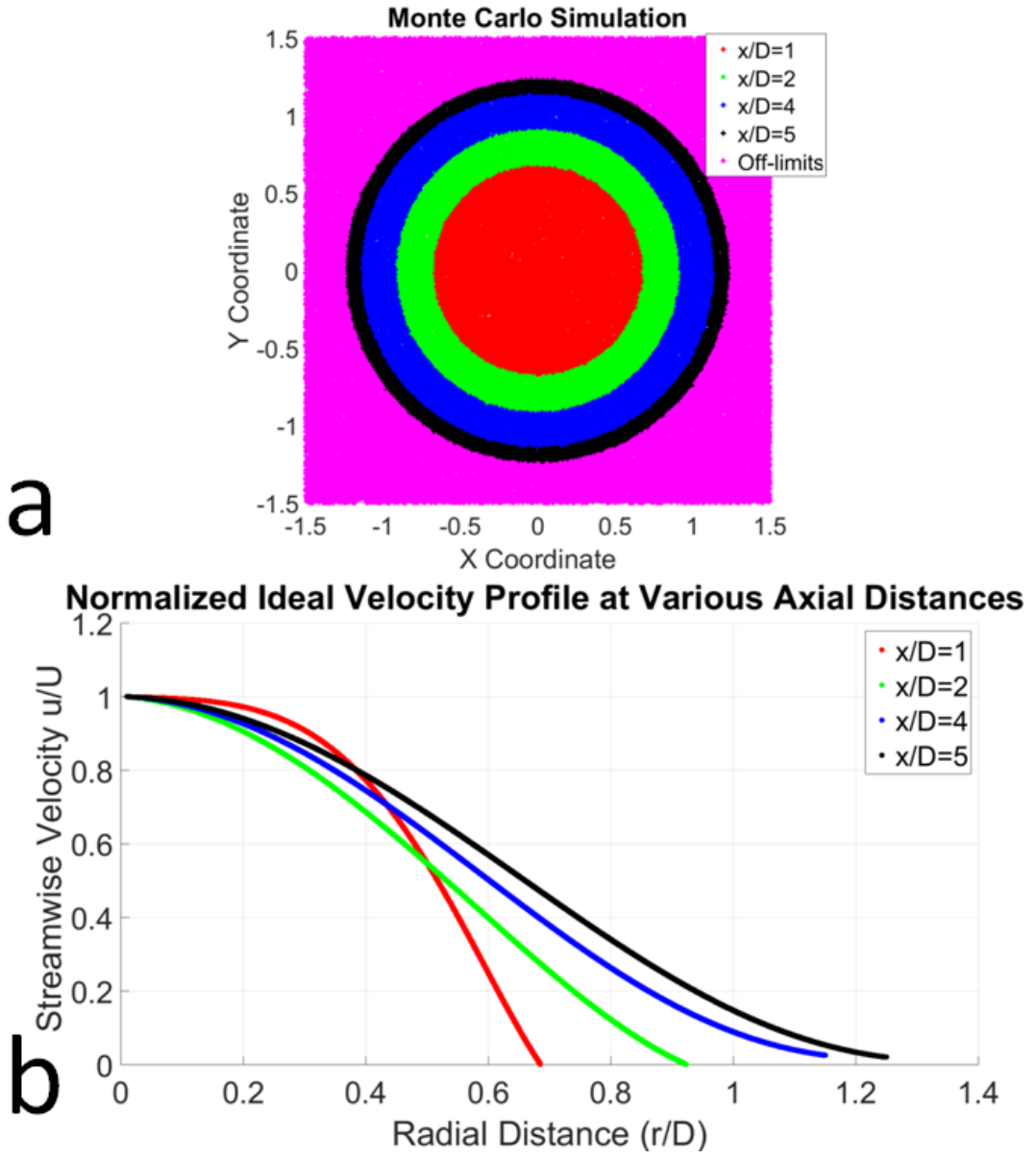

Figure 4.4: (a) The Monte Carlo simulation scatter plot generated with 100,000 samples. The colors represent the various axial distances. (b) The velocity profiles at various axial distances obtained from the polynomial fitted curves of the data obtained from Fellouah et al.

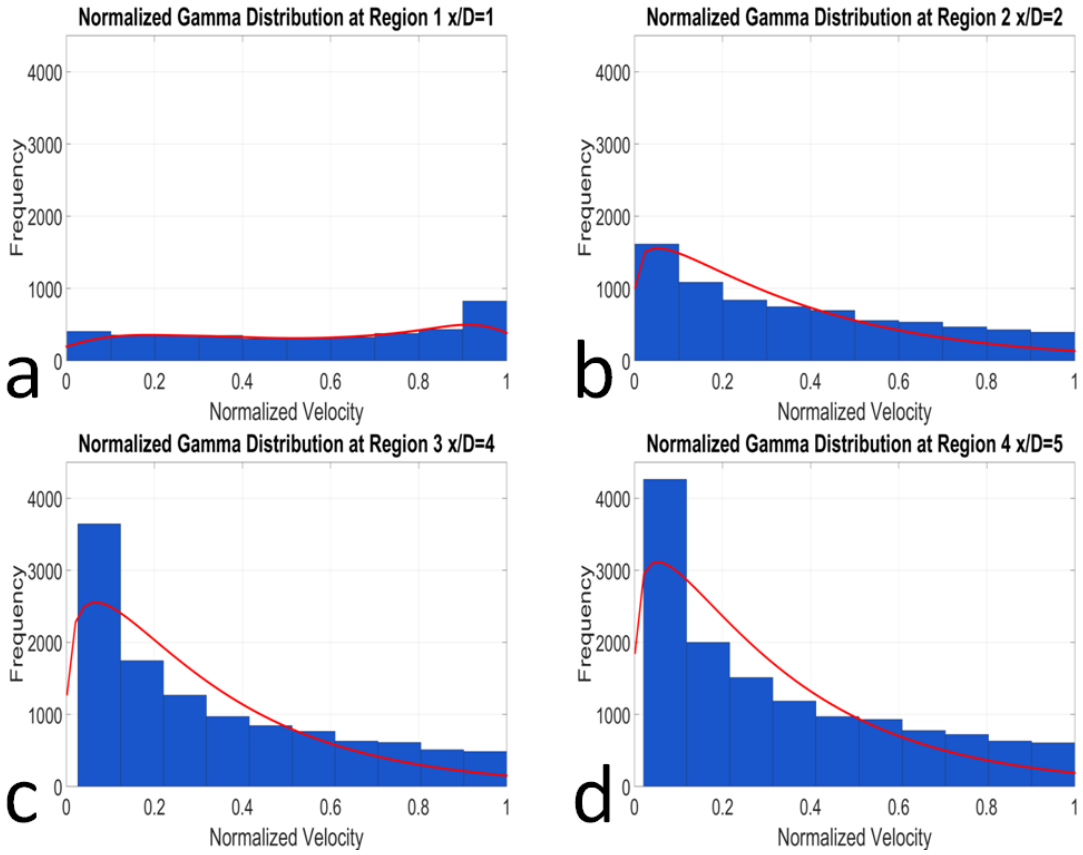

Figure 4.5: Normalized streamwise velocity histograms and the fitted gamma distribution curve for (a) region 1, (b) region 2, (c) region 3 and (d) region 4.

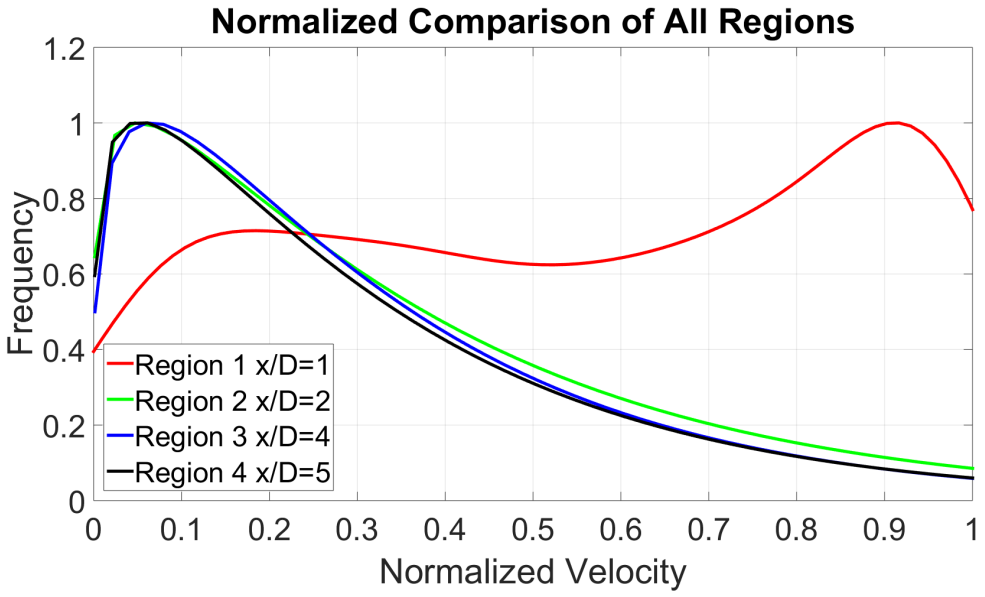

Figure 4.6: Comparison of all normalized regions with fitted gamma distribution curves superimposed from the reference Monte Carlo simulation.

4.2 Helium jet

No baseline velocity for the helium jet was able to be measured here. Attempts were made to perform PIV, but no adequate seeding of the flow could be achieved. The available wand anemometer did not have sufficient time resolution and was too large for accurate measurements. The goal of this thesis work was to determine whether the properties of the turbulent features could be calculated to visualize the deformation over a series of frames, which can be accomplished without an absolute measurement of the velocity profile. Thus the Monte Carlo simulated velocity histograms are used for comparison with normalized velocities.

The velocity measurements of each region of interest for the helium jet are all normalized by the local region maximum. For the helium jet the trends are similar in terms of skewness of the fitted gamma curves with the exception of region 1 as shown in Figure 4.7. The region 1 curve was expected to be skewed to the right, but this was not observed, which is most likely due to the helium jet core which has the highest velocity has not become fully turbulent yet, and thus is not imaged or measured with SIV. The comparison of all the fitted gamma distribution curves follow similar trends to those of the Monte Carlo simulation as shown in Figure 4.8 were the curves begin to collapse to a single point.

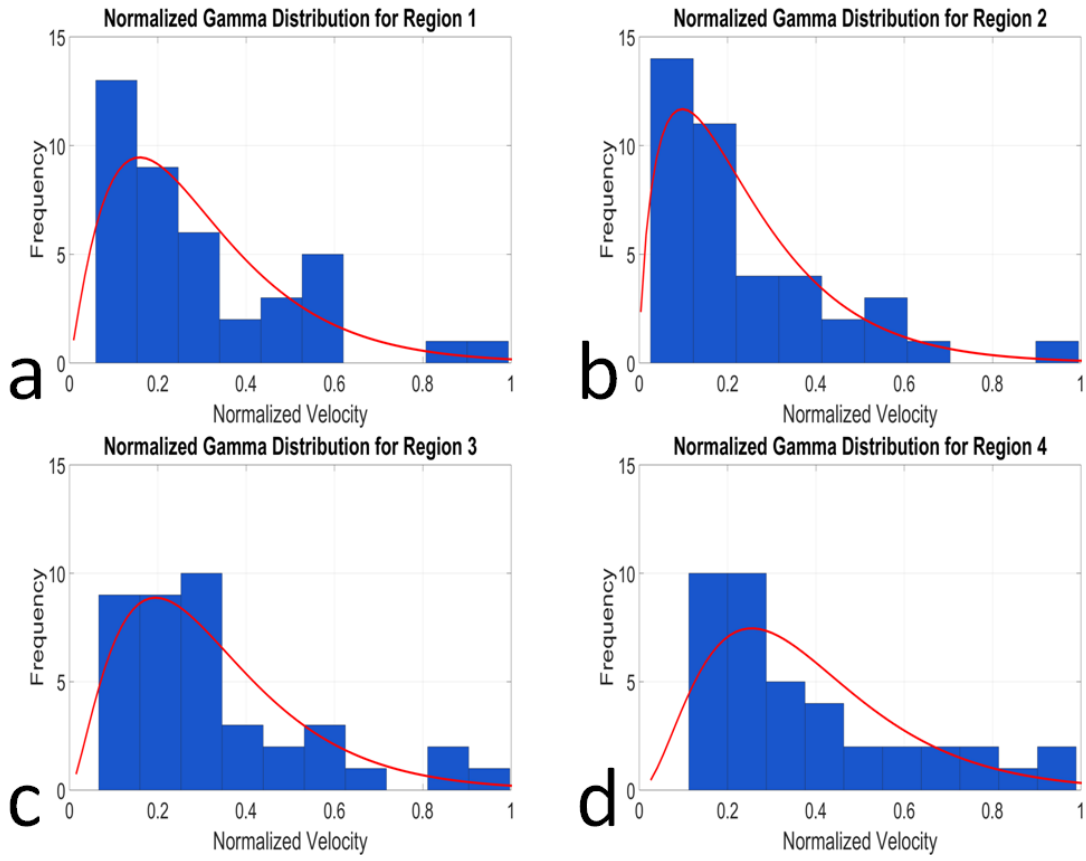

Figure 4.7: Normalized velocity histograms and the fitted gamma distribution curves of the helium jet with a vertical cutoff for (a) region 1, (b) region 2, (c) region 3 and (d) region 4.

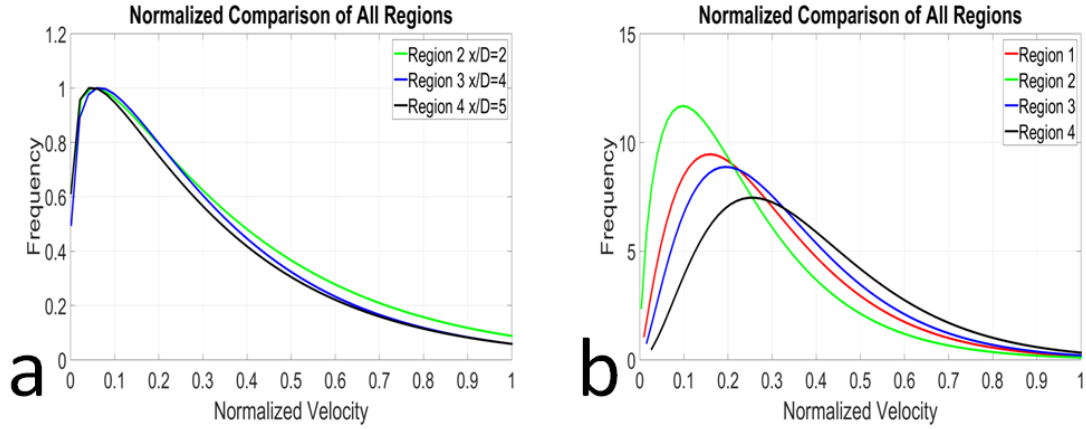

Figure 4.8: Comparison of all normalized regions with fitted gamma distribution curves superimposed for the (a) ideal velocity histogram using the Mont Carlo simulation and the (b) velocity histogram for the helium jet with a vertical cutoff.

4.3 JetCat P80-SE Micro-turbine

For the analysis of the JetCat P80-SE there were four regions of interest selected, the four regions are superimposed on the raw schlieren images for each cutoff variation as shown on Figure 4.2. For each data set, 16 to 24 frames were used for each data set to obtain 20 features per regions of interest from the black and white data sets. The velocity measurements of each region of interest presented are all normalized by the local region maximum. This test platform was used to compare the effect of schlieren cutoff on the SIV measurements, the difference between this testbed and all others is that it is not a single jet, but an annular region.

The images produced by the circular cutoff had large features that appeared to be strands that oscillated near the edges of the exhaust plume as shown in Figure 4.2 a. Visually the features displayed excessive noise which made it difficult to distinguish the texture within the exhaust plume from the background, compared to the images of the other cutoff variations. The images from the horizontal cutoff produced similar characteristics to those of the circular cutoff where the turbulent features were large and appeared to oscillate. Although the features were concentrated towards the center of the exhaust plume, as opposed to the edges as shown in Figure 4.2 b. When focused shadowgraph (no cutoff) was used the turbulent features were smaller and more consistent in size as shown in Figure 4.2 c, the turbulent feature movement was also more apparent and moved in the direction of the flow. The vertical cutoff shown in Figure 4.2 d produced images were the turbulent features were larger, but also better defined when compared to the other cutoff variations.

4.3.1 Circular cutoff

When the individual histograms and fitted gamma distribution curves are compared to each other they demonstrate similarity in skewness as shown in Figure 4.9. When the fitted curves were superimposed, the trends in the circular cutoff show similarities to those in the free air jet Monte Carlo in terms of skewness. The progression of the fitted gamma distribution curves for the micro-turbine did not match the sequence observed in the Monte Carlo jet data as shown in Figure 4.10. This is likely due to the jet turbine being an annular jet instead of a simple free jet.

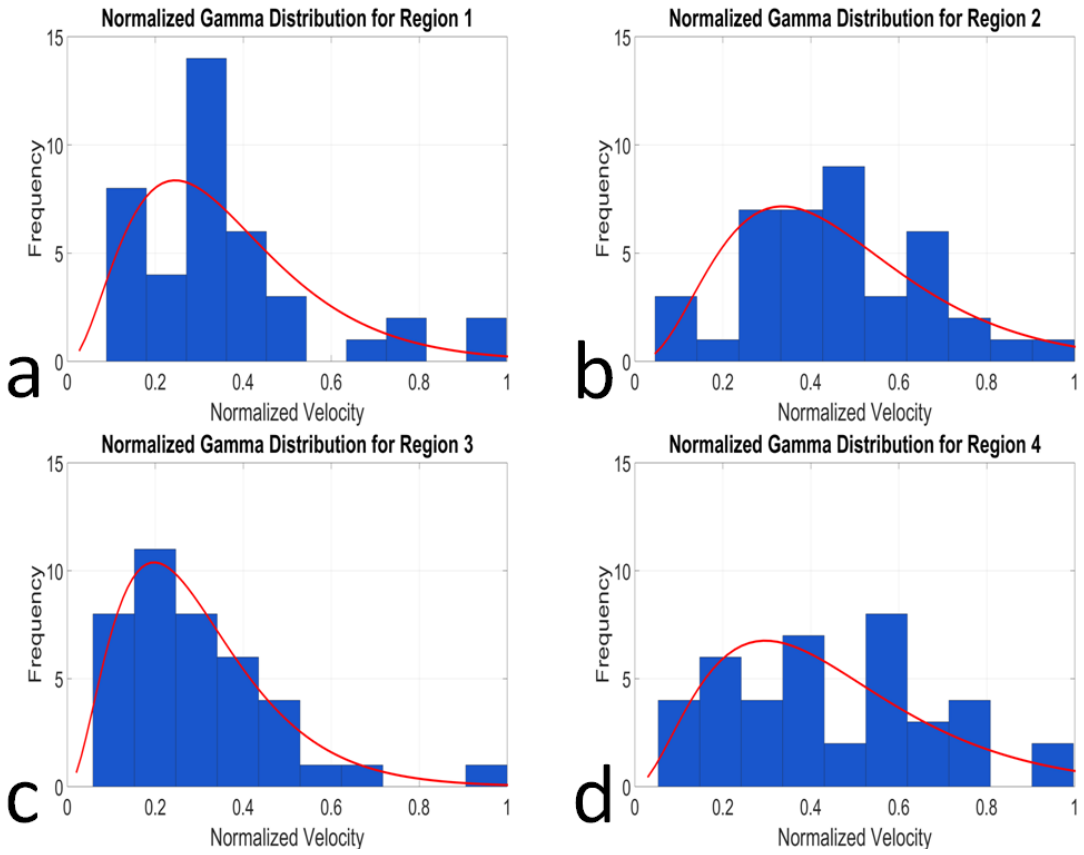

Figure 4.9: Normalized velocity histograms and the fitted gamma distribution curves of the JetCat P80-SE micro-turbine with a circular cutoff for (a) region 1, (b) region 2, (c) region 3 and (d) region 4.

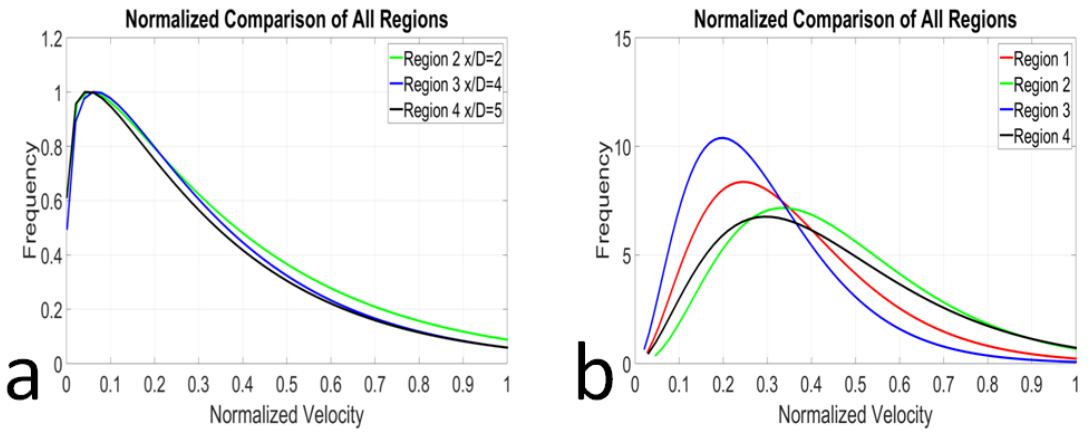

Figure 4.10: Comparison of all normalized regions with fitted gamma distribution curves superimposed for the (a) ideal velocity histogram using the Mont Carlo simulation and the (b) Velocity histogram for the JetCat P80-SE microturbine with a circular cutoff.

4.3.2 Horizontal cutoff

When the individual histograms and fitted gamma distribution curves are compared to each other they demonstrate similarity in skewness with variations in the peakedness as shown in Figure 4.11. When the fitted curves are superimposed and compared to those in the free air jet as shown in Figure 4.12, there are similarities to those in the free air jet in regions 2 and 3.

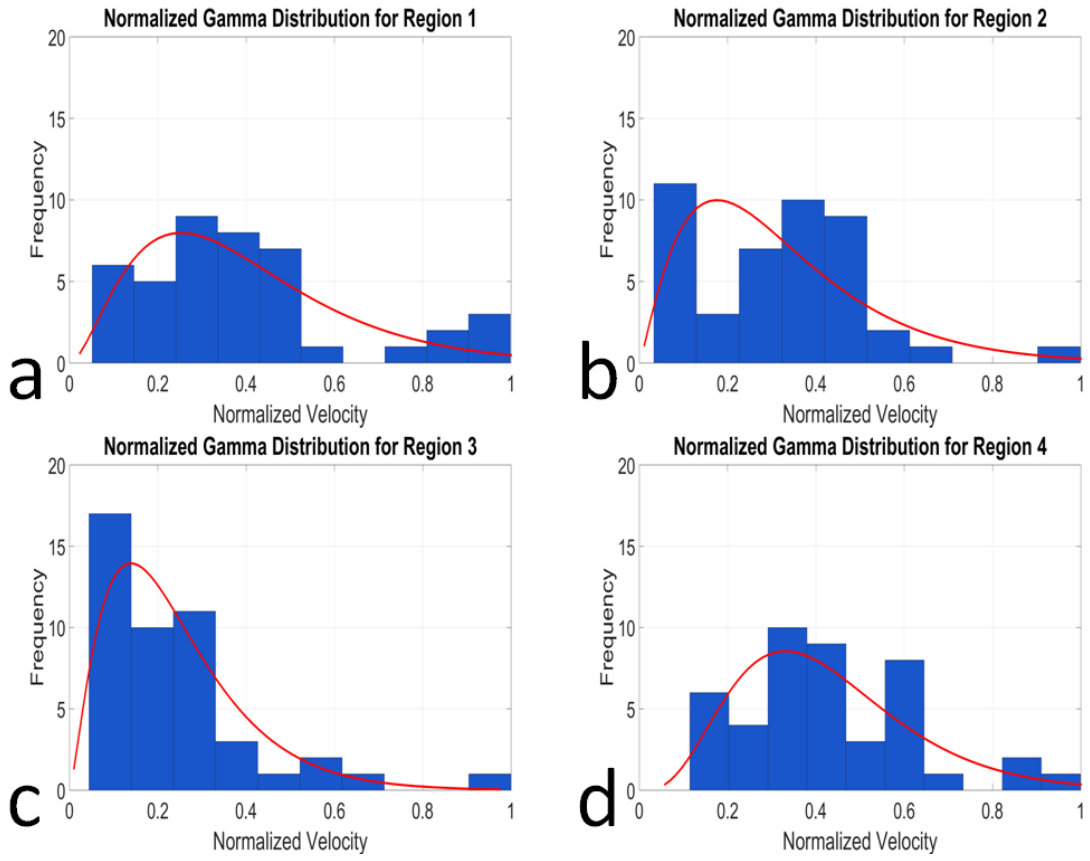

Figure 4.11: Normalized velocity histograms and the fitted gamma distribution curves of the JetCat P80-SE micro-turbine with a horizontal cutoff for (a) region 1, (b) region 2, (c) region 3 and (d) region 4.

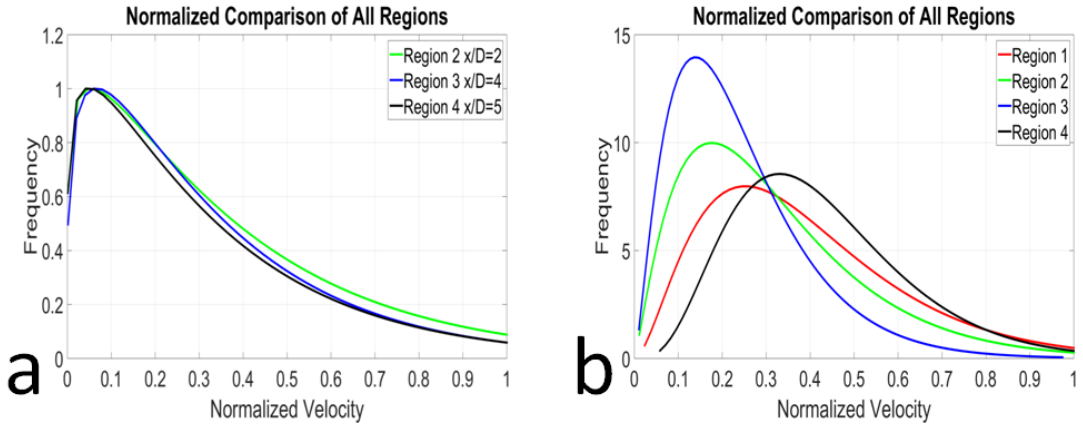

Figure 4.12: Comparison of all normalized regions with fitted gamma distribution curves superimposed for the (a) ideal velocity histogram using the Mont Carlo simulation and the (b) Velocity histogram for the JetCat P80-SE microturbine with a horizontal cutoff.

4.3.3 Focused shadowgraph

When the individual histograms and fitted gamma distribution curves are compared to each other they demonstrate similarity in skewness with variations in peakedness as shown in Figure 4.13. When the fitted curves are superimposed, the curves show a transition from right to left, which show the velocity decrease. The trends from the focused shadowgraph in Figure 4.14 show some similarities to those of the Monte Carlo simulation as the curves begin to collapse to a single point.

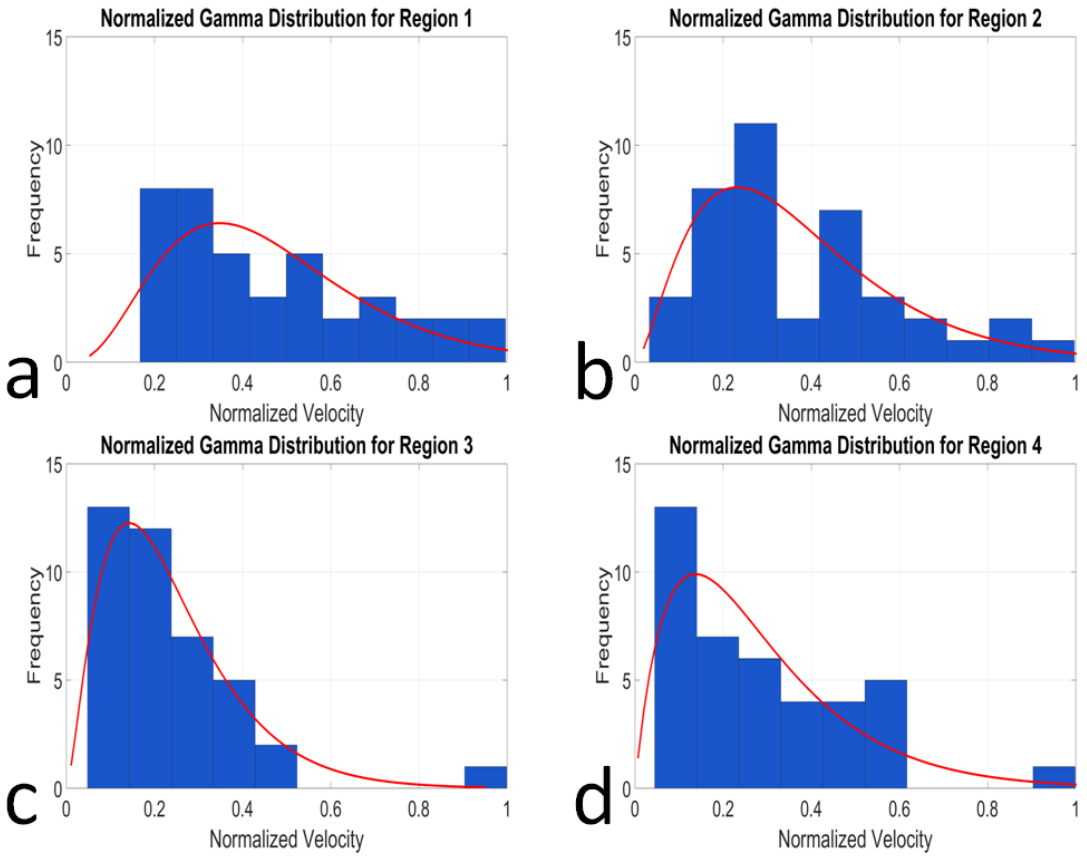

Figure 4.13: Normalized velocity histograms and the fitted gamma distribution curves of the JetCat P80-SE micro-turbine with focused shadowgraph (no cutoff) for (a) region 1, (b) region 2, (c) region 3 and (d) region 4.

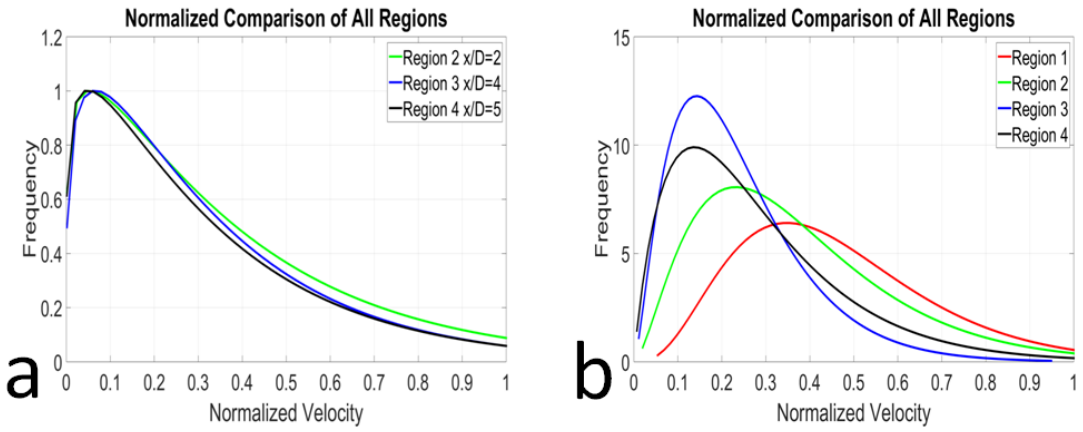

Figure 4.14: Comparison of all normalized regions with fitted gamma distribution curves superimposed for the (a) ideal velocity histogram using the Mont Carlo simulation and the (b) Velocity histogram for the JetCat P80-SE microturbine with focused shadowgraph (no cutoff).

4.3.4 Vertical cutoff

When the individual histograms and fitted gamma distribution curves are compared to each other they demonstrate similarity in skewness with variations in the peakedness as shown in Figure 4.15. When the fitted curves are superimposed and compared to those of the Monte Carlo simulation as shown in Figure 4.16, there are similarities in terms of skewness, but variations in peakedness.

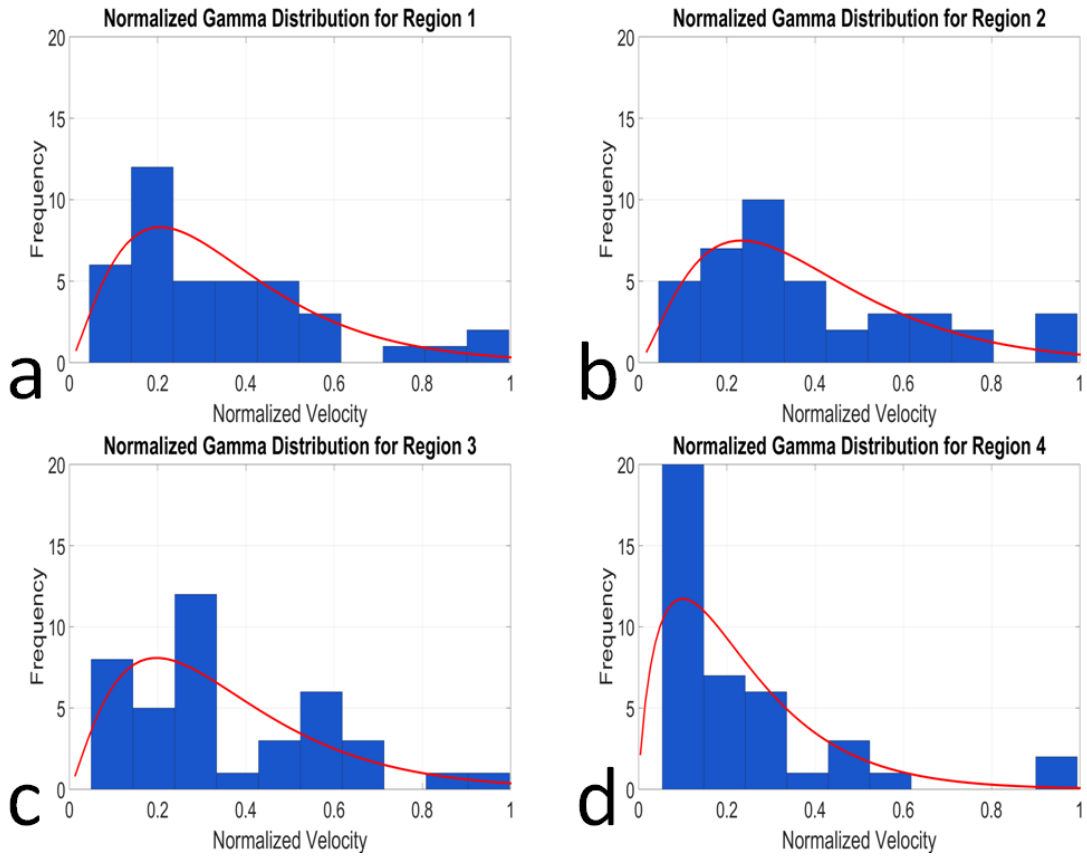

Figure 4.15: Normalized velocity histograms and the fitted gamma distribution curves of the JetCat P80-SE micro-turbine with a vertical cutoff for (a) region 1, (b) region 2, (c) region 3 and (d) region 4.

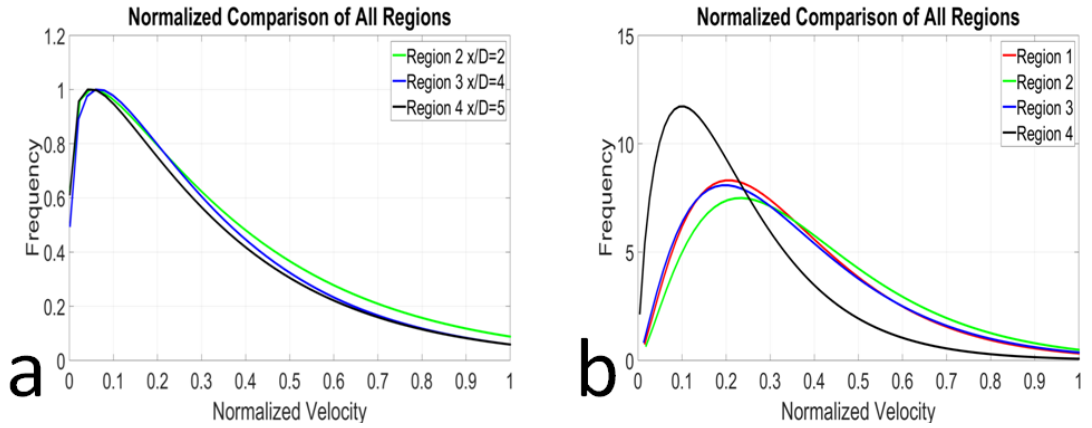

Figure 4.16: Comparison of all normalized regions with fitted gamma distribution curves superimposed for the (a) ideal velocity histogram using the Mont Carlo simulation and the (b) Velocity histogram for the JetCat P80-SE micro-turbine with a vertical cutoff.

4.3.5 Discussion

From the micro-turbine and cutoff variations the the circular and horizontal cutoff provided partial flow field visualization, while the focused shadowgraph and vertical cutoff provided full field visualization as shown in Figure 4.17. The circular cutoff focused on the turbulent features near the edges and not near the exit plane, which may be due to the annular design of the micro-turbine. The horizontal cutoff provided a gradient in the the radial direction, which may be due to setup error since the graident is not consistent in the axial direction. The vertical cut off produced a gradient in the axial direction and provided large turbulent features, which facilitated the tracking process. The focused shadowgrpah performed similar to the vertical cutoff, but the turbulent features were more consistent and smaller in size.

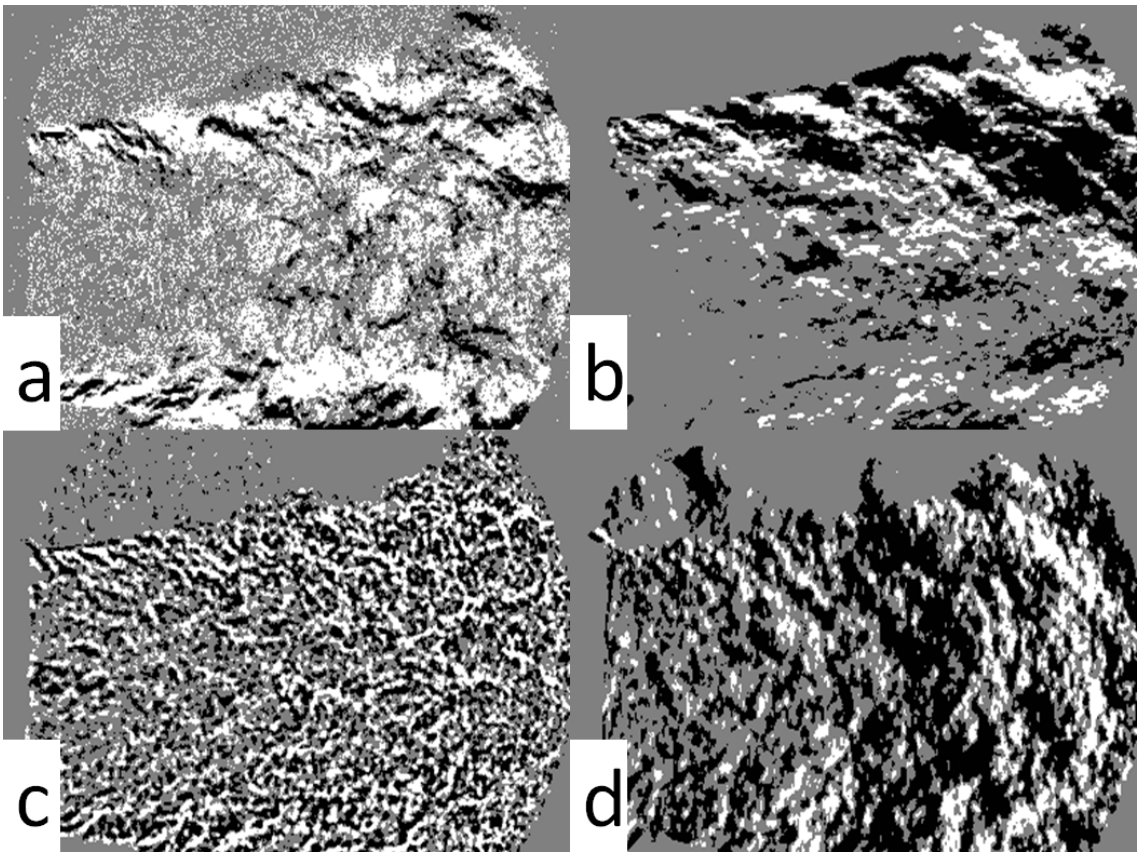

Figure 4.17: Processed images of the JetCat P80-SE micro-turbine with a (a) circular cutoff, (b) horizontal cutoff, (c) focused shadowgraph (no cutoff) and (d) vertical cutoff.

4.4 Small-scale liquid rocket engine

The small-scale liquid rocket engine consisted of two tests one with a vertical cutoff and another with focused shadowgraph. Data was obtained from the manual turbulent feature tracking of the vertical cutoff but could not be performed for the focused shadowgraph due to the spatial resolution as discussed below.

4.4.1 Vertical cutoff

When the histogram and fitted gamma distribution curves are compared to each other there are similarities in the curves as they skew to the left, but show

variations in peakedness as shown in Figure 4.18. When all the fitted gamma distribution curves are superimposed region 2 and 3 are very similar, which demonstrate similar trends to those of the Monte Carlo simulation as shown in Figure 4.19.

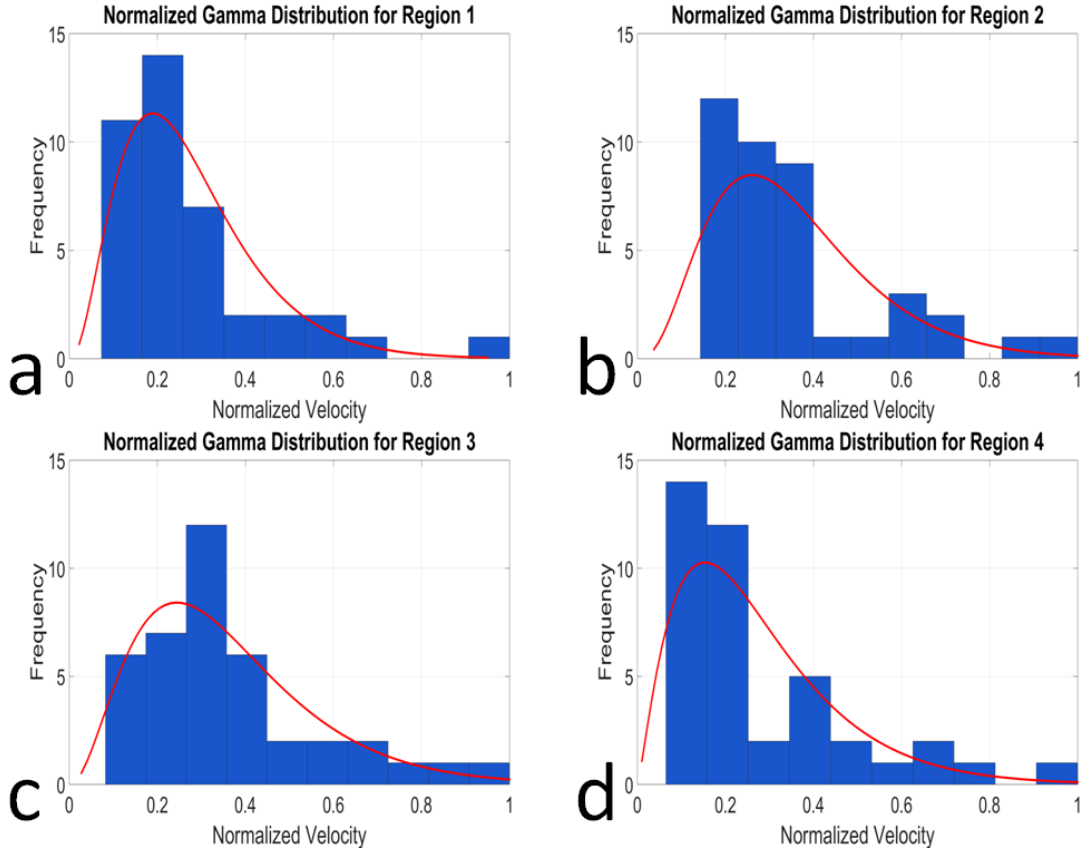

Figure 4.18: Normalized velocity histograms and the fitted gamma distribution curves of the small-scale liquid rocket engine test 1 with a vertical cutoff for (a) region 1, (b) region 2, (c) region 3 and (d) region 4.

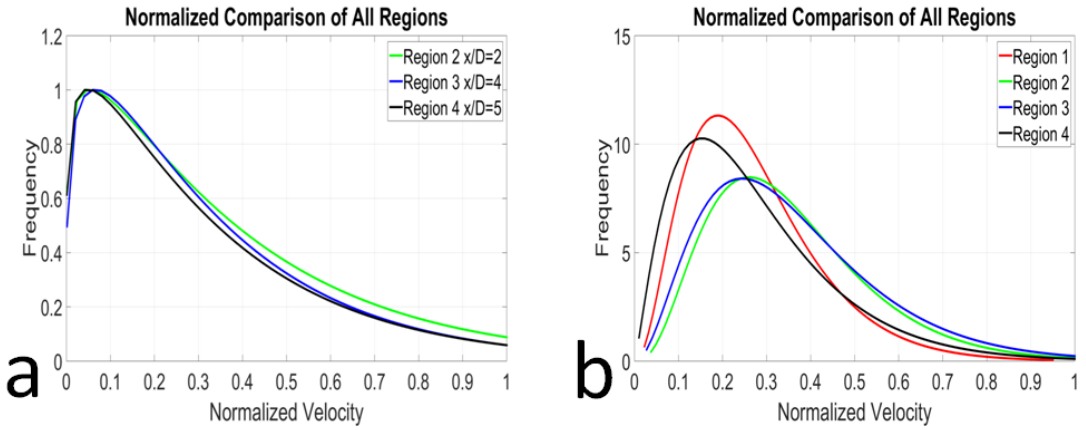

Figure 4.19: Comparison of all normalized regions with fitted gamma distribution curves superimposed for the (a) ideal velocity histogram using the Mont Carlo simulation. (b) The Velocity histogram for the the small-scale liquid rocket engine test 1 with a vertical cutoff.

An ideal velocity profile was constructed with published data for a compressible jet that was obtained with a hot-wire anemometers rake positioned in the center of the jet [30]. SIV provides 2D path average velocity measurements of the axisymmetric flow, the comparison of the path average and center-plane velocities was made with the Abel transform [12]. The Abel transform was applied to the ideal velocity profile to reconstruct the path-averaged velocity as shown in equation 4.2, were it is applied from the edge to the center of the jet. The path-averaged velocity is reconstructed by the sum of the planar velocity measurements divided by the number of velocity measurements at the location *(i,j)*.

$$V_{path-averaged}(i,j) = \frac{\sum_{i_{edge}}^{i_{center}} V_{planar}(i,j)}{N_{i_{edge} \rightarrow i_{center}}} \tag{4.2}$$

The theoretical velocity at the exit plane provided by NASA CEA was combined with the Monte Carlo simulation to construct an ideal velocity profile at region 3. Region 3 of the SIV analysis was selected due to the limited number of velocity measurements available. The trend of the velocity profile from the SIV analysis demonstrates similarities to that of the of the velocity profile constructed by the Abel transform as shown in Figure 4.20, were u is the velocity and U is the local maximum velocity. The maximum velocity measurements are shown in Table 4.2 for the NASA CEA theoretical results combined with the Monte Carlo simulation, the Abel transform and the SIV analysis.

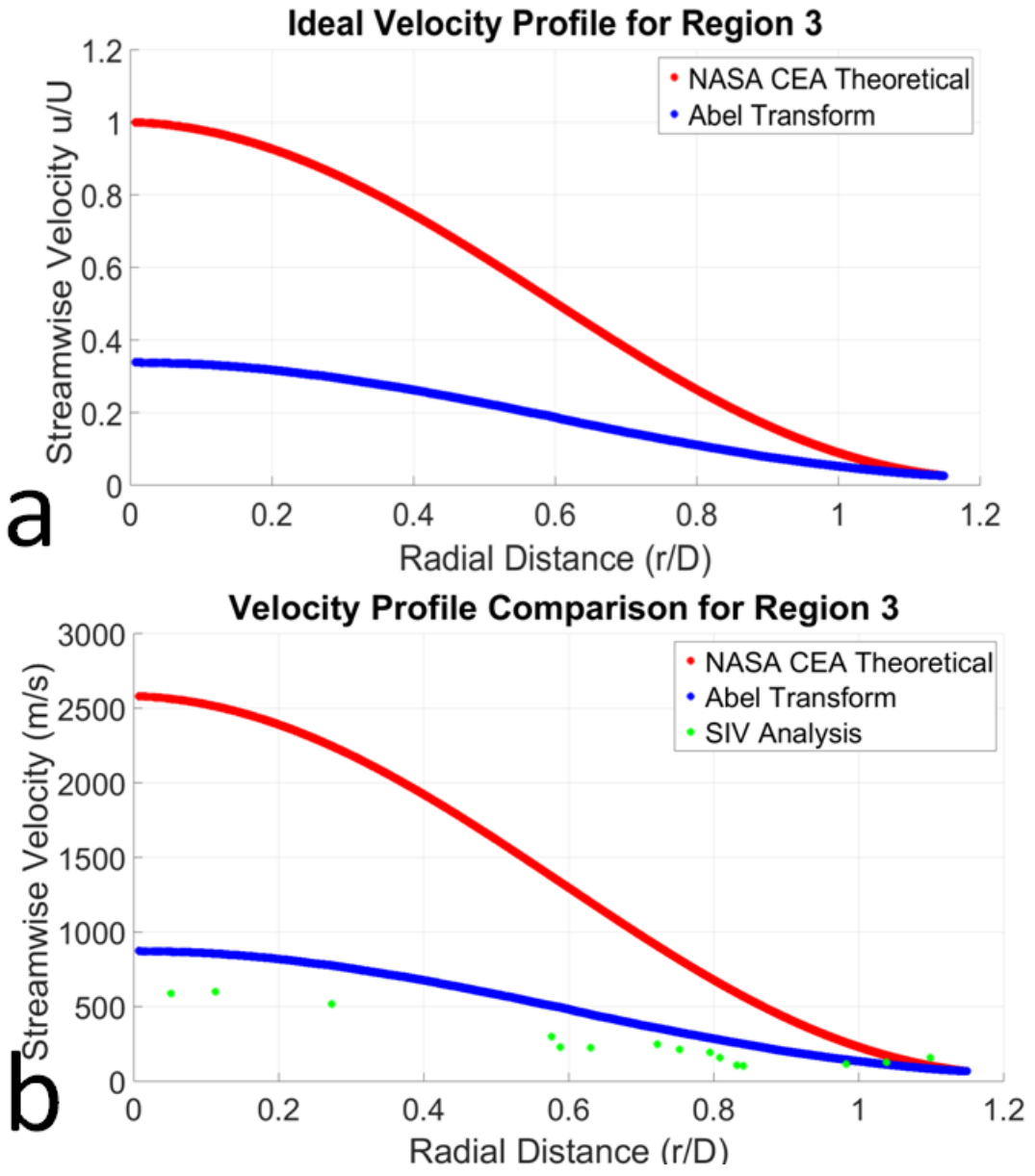

Figure 4.20: (a) Ideal velocity profile for region 3 and (b) the comparison of the ideal velocity profiles and the SIV analysis.

Table 4.2: Comparison of the maximum velocities of all the velocity profiles at region 3 for test 1.

Velocity profile	Maximum velocity
NASA CEA Theoretical	2,577 m/s
Abel Transform	872 m/s
SIV Analysis	590 m/s

4.4.2 Focused shadowgraph (no cutoff)

The velocity measurements for the small-scale liquid rocket engine test 2 using focused shadowgraph (no cutoff) were not performed due to the small turbulent feature sizes. The focused shadowgraph images were captured with a spatial resolution of 384x160 and produced a majority of small turbulent features as shown in Figure 4.21. The combination of the low spatial resolution and small turbulent features sizes made manual tracking challenging and unreliable, therefore the manual turbulent feature tracking was not performed on that data set. When a small size filter was applied and the images superimposed the turbulent features were congested and difficult to track. When the size filter was increased there were fewer turbulent features present and almost no matching turbulent features found as shown on Figure 4.22.

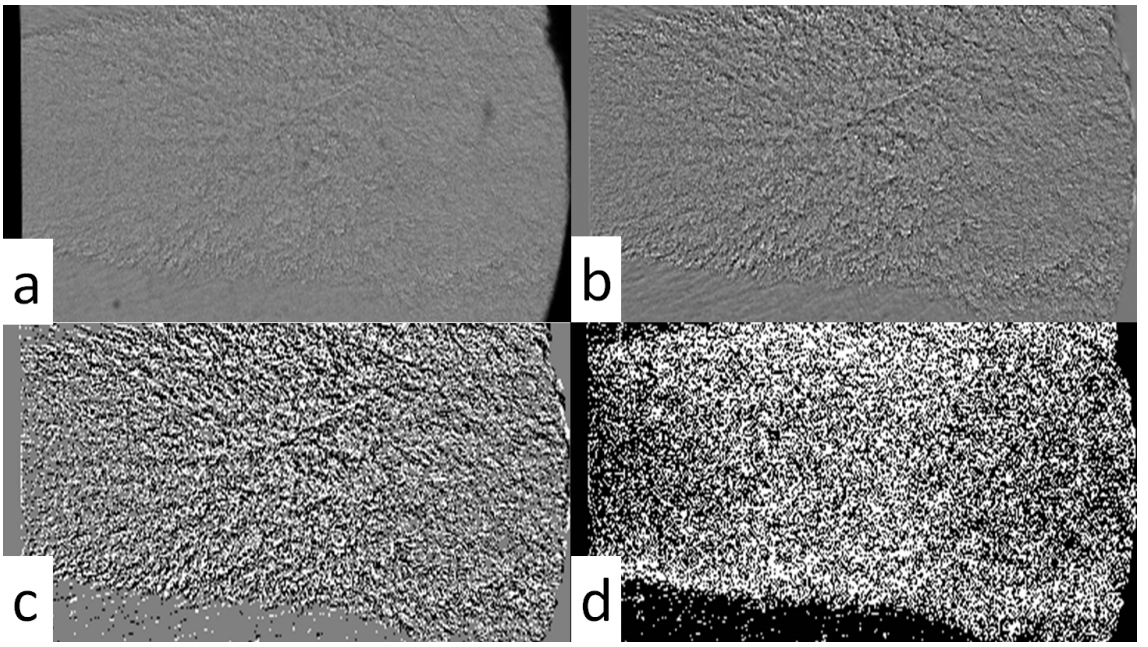

Figure 4.21: Images from the rocket test 2, (a) raw schlieren image, (b) background subtraction, (c) and multi-level threshold. (d) Binary conversion, were all black and white pixels are turned into white and gray pixels are turned into black.

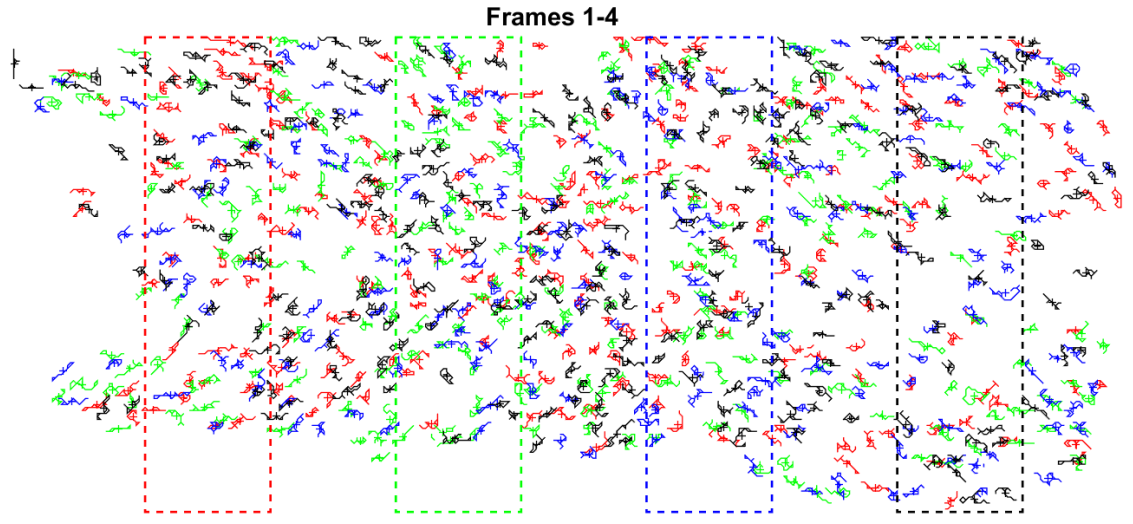

Figure 4.22: 4 sequential frames of the white turbulent features from the rocket test 2 superimposed with an area filter of 10 to 20 pixels in area. The combination of the small turbulent features and spatial resolution made manual turbulent feature tracking difficult to perform.

CHAPTER 5

CONCLUSION AND SUGGESTIONS FOR FUTURE RESEARCH

5.1 Conclusion

The focus of this research work has been to develop image processing methods to identify individual turbulent features in jets, visualized with refractive imaging. Images via schlieren visualization show turbulent features of various sizes at different regions through out the flow field which move and deform at various rates. Coherent turbulent features, which retain their shape with minimal deformation, were of particular interest here to obtain velocity measurements. Manual turbulent feature tracking was performed due to limitations in the automation of a pattern recognition and path construction MATLAB script to correlate turbulent features.

Image processing methods developed incorporated background subtraction to eliminate the background noise and imperfections in the optical equipment. The multilevel threshold developed allowed for the visualization of the light and dark turbulent features while differentiating the background from the turbulent features. Methods were developed to reconstruct a new image showing only turbulent features of a limited size range, which facilitated the tracking process.

The choice of schlieren cutoff affects the ability to track turbulent features through images. The trends produced by the focused shadowgraph and vertical cutoff demonstrated closer similarities to the free air jet with the Monte Carlo simulation. The focused shadowgraph images produced smaller turbulent features that show potential for automation since they are smaller and more consistent in size when compared to all other variations. The vertical cutoff shows larger turbulent features that are visually easier to track but may introduce error if automated, since it may enclose parts of other turbulent features.

While SIV shows the capability of tracking turbulent features, more velocity measurements are needed to obtain a more definite conclusion. The skewness in the fitted gamma curves demonstrate more similarities than the peakedness, when the testbeds are compared to the free air jet. The peakedness of the curve is affected by the number of samples and in order to address this issue more velocity measurements are needed.

Comparison between the SIV data and an approximation of the rocket exhaust velocity profile show comparable results. The results indicate that with additional measurements and automation of the tracking process, the center-plane velocity profile of the exhaust plumes can be reconstructed. The center-plane velocity profile can be obtained through the application of the Abel transform since schlieren images provide a 2D path average of the axisymmetric flow.

5.2 Future research suggestions

The main recommendation for future research is the compilation of the individual image processing codes for automation of the turbulent feature matching. Currently there are multiple codes that each require intensive user input, which introduces human error into the process. The compilation and automation process will require extensive computer programming. The possibility of compiling the codes into a graphical user interface (GUI) would also make the script more user friendly.

The image processing methods presented here can be used to identify and isolate turbulent features, the next steps would be to match the feature between a series of frames. While manual turbulent feature tracking is feasible it is also tedious and introduces human error. A suggestion for the automation of the MATLAB script would be using the built in function *normxcorr2*. Ideally a coherent turbulent feature should undergo minimal deformation so the centroid would have minimal effects and accurately capture the translation of the turbulent feature. This would mitigate the need for an advanced correlation algorithm.

The function *normxcorr2* identifies the position of best fit using a normalized correlation coefficient. A window is selected from an image called a template and is used to match in another image by matching the most normalized intensities in the matrix of another image [32]. With a known location of the turbulent feature, a box can be used to isolate the feature and then translated in the next frame to identify a matching position of best fit as shown on Figure 5.1. The dynamic search window may reduce the possibility of background noise by focusing on the turbulent features. The use of a dynamic window is also suggested, due to the difficulty in categorizing the turbulent features in to a consistent size to assign a fixed region of interest.

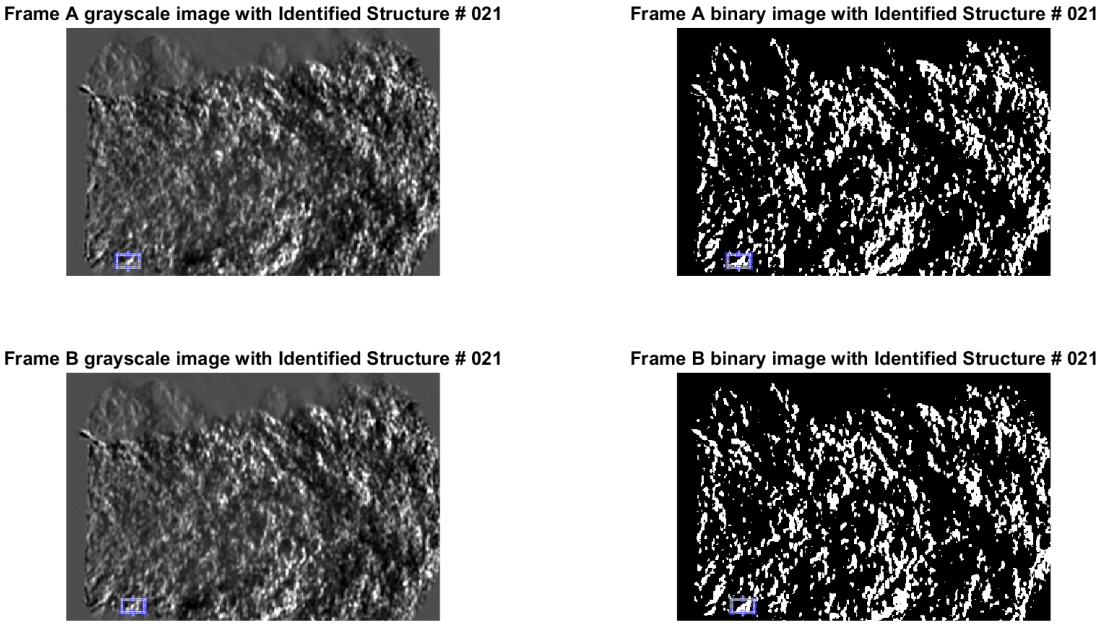

Figure 5.1: Example of the *normxcorr2* function in MATLAB, were the turbulent feature has been identified in one frame and matched in the subsequent frame.

There are two methods suggested to perform the automation of the turbulent feature tracking. The first method is to isolate individual features from the first image and use those as templates to match in the subsequent frame. The other method is to isolate and extract turbulent features from two frames and to determine which pair provides the best match. If the turbulent feature matching is performed in the gray scale images the focus will be on the interior features, since the pixel intestines within the features provide a unique texture. If it is performed in a binary images the focus will be on the exterior features, since the interior of the features will be of all the same intensities.

REFERENCES

[1] Mounia Belmouss. Effect of electrode geometry on high energy spark discharges in air. Master's thesis, Purdue University, West Lafayette IN, 2015.

[2] Roberto Sosa, Elise Arnaud, Étienne Mémin, and Guillermo Artana. Schlieren image velocimetry applied to ehd flow. *International Symposium on Electrohydrodynamics*, 2006.

[3] Yunus A. Cengel and John M. Cimbala. *Fluid Mechanics: Fundamentals and Applications*. McGraw-Hill, New York NY, 3rd edition, 2014.

[4] Markus Raffel, Christian E. Willert, Steve T. Wereley, and Jurgen Kompenhans. *Particle Image Velocimetry A Practical Guide*. Springer Berlin Heidelberg, Germany, 2nd edition, 2007.

[5] Gary S. Settles. *Schlieren and Shadowgraph Techniques: Visualizing Phenomena in Transparent Media*. Springer-Verlag Berlin, Germany, 2001.

[6] S Tokgoz, R Geisler, L J A van Bokhoven, and B Wieneke. Temperature and velocity measurements in a fluid layer using background-oriented schlieren and PIV methods. *Measurement Science and Technology*, 23(11):115302, 2012.

[7] Michael J. Hargather. Background-oriented schlieren diagnostics for large-scale explosive testing. *Shock Waves*, 23(5):529–536, 2013.

[8] Michael J. Hargather and Gary S. Settles. Retroreflective shadowgraph technique for large-scale flow visualization. *Applied Opics.*, 48(22):4449–4457, Aug 2009.

[9] Michael J. Hargather, Michael J. Lawson, Gary S. Settles, and Leonard M. Weinstein. Seedless velocimetry measurements by schlieren image velocimetry. *AIAA Journal*, 49(3):611–620, 2011.

[10] Sayan Biswas and Li Qiao. A comprehensive statistical investigation of schlieren image velocimetry (SIV) using high-velocity helium jet. *Experiments in Fluids*, 58(3), 2017.

[11] Michael J. Hargather, Gary S. Settles, and Sivaram Gogineni. Optical diagnostics for characterizing a transitional shear layer over a supersonic cavity. *AIAA Journal*, 51(12):2977–2982, 2013.

[12] Dennis R. Jonassen, Gary S. Settles, and Michael D. Tronsky. Schlieren "PIV" for turbulent flows. *Optics and Lasers in Engineering*, 44(3-4):190–207, 2006.

[13] Sivaram Gogineni and Chol-Bum Kweon. Focused-schlieren-based seedless velocimetry for spray and combustion studies. Technical report, Spectral Energies LLC, Dayton OH, 2014.

[14] Emishaw D. Iffa, A. Rashid A. Aziz, and Aamir S. Malik. Velocity field measurement of a round jet using quantitative schlieren. *Applied Optics*, 50(5):618–625, Feb 2011.

[15] George Papadopoulos. Shadow image velocimetry (SIV). *Symposium on Technology for the Next Century*, 1999.

[16] Jason A. Volpe and Gary S Settles. Laser-induced gas breakdown as a light source for schlieren and shadowgraph particle image velocimetry. *Optical Engineering*, 45, 08 2006.

[17] Elise Arnaud, Etienne Mémin, Roberto Sosa, and Guillermo Artana. A fluid motion estimator for schlieren image velocimetry. *Computer Vision – ECCV 2006 Lecture Notes in Computer Science*, pages 198–210, 2006.

[18] H. C. H. Townend. A method of air flow cinematography capable of quantitative analysis. *Journal of the Aeronautical Sciences*, 3(10):343–352, 1936.

[19] Gary S. Settles and Michael J Hargather. A review of recent developments in schlieren and shadowgraph techniques. *Measurement Science and Technology*, 28(4):042001, 2017.

[20] Engineering ToolBox. Gases - density. $https://www.engineeringtoolbox.com/gas-density-d_158.htm$, 2003. Last accessed 02/30/2018.

[21] JetCat. Jetcat RX turbine with V10 ECU. Technical report, JetCat.

[22] Stewart H. Youngblood. Design and testing of a liquid oxide and ethanol fueled rocket engine. Master's thesis, New Mexico Institute of Mining and Technology, Socorro, NM, 2015.

[23] NASA. Chemical equilibrium with application. Accessed: 2018-06-02.

[24] George P. Sutton and Oscar Biblarz. *Rocket Propulsion Elements*. Wiley, Hoboken NJ, 8 edition, 2010.

[25] Nobuyuki Otsu. A threshold selection method from gray-level histograms. *IEEE Transactions on Systems, Man, and Cyberneticss*, 9(1):62–66, 1979.

[26] Rafael C. Gonzalez, Richard E. Woods, and Steven L. Eddins. *Digital Image Processing Using MATLAB*. Gatesmark Publishing, Knoxville TN, 2 edition, 2009.

[27] P. T. Tokumaru and P.E Dimotakis. Image correlation velocimetry. *Experiments in Fluids*, 19(1):1–15, 1995.

[28] Douglas C. Montgomery and George C.Runger. *Applied Statistics and Probability for Engineers*. Wiley, Hoboken, NJ, 6th edition, 2014.

[29] Ken Black. *Business Statistics: for Contemporary Decision Making*. John Wiley and Sons, Hoboken, NJ, 6th edition, 2010.

[30] H. Fellouah, C.G. Ball, and A. Pollard. Reynolds number effects eithin the development region of a turbulent round free jet. *International Journal of Heat and Mass Transfer*, 52(17):3943 – 3954, 2009.

[31] Richard A. Johnson, Irwin Miller, and John E. Freund. *Miller and Freund's Probability and Statistics for Engineers*. Pearson Education, Inc., Boston, MA, 2018.

[32] J. P. Lewis. Fast normalized cross-correlation. Technical report, Vision Interface, 1995.

LAGRANGIAN SCHLIEREN IMAGE VELOCIMETRY MEASUREMENTS IN EXHAUST PLUMES

by

RUDY MORALES